5-2020

Synthesizing and modeling the optical properties of silica aerogel

Hannah Margavio
University of Tennessee at Chattanooga, lxf841@mocs.utc.edu

Synthesizing and Modeling the Optical Properties of Silica Aerogel

Hannah Rose Marie Margavio

Departmental Honors Thesis
University of Tennessee at Chattanooga
Chemical Engineering

Examination Date: March 27th, 2020

Dr. Sungwoo Yang
Assistant Professor of Chemical Engineering
Thesis Direction

Dr. Louie Elliott
Assistant Professor of Mechanical Engineering
Department Examiner

Table of Contents

Introduction

Silica aerogel has attracted the attention of researchers for decades for its applications in insulation materials, storage, and solar-thermal devices. The first synthesis process was discovered in the early 1930's by Samuel Kistler who synthesized silica, alumina, tungstic oxide, gelatin, and other aerogels. Kistler's synthesis was founded on the basis of removing water and other solvents from hydrogels and alcogels [1]. The appeal surrounding silica aerogel is attributed to its unique combination of physical and chemical properties. Silica aerogel is a highly porous (~80-99.98%) [2], optically transparent nano-polymer with a low thermal conductivity (0.005 W/m-K) [1]. Additionally, the material boasts a super-low density (0.003-0.3 g/cm^3) [1], high specific surface area (500-1200 m^2/g) [2], and low dielectric constant [3]. The following report proposes a viable method of synthesizing polyvinylpolymethylsilane (PVPMS) aerogel as well as a model for determining the optical performance of TMOS aerogel by determining its radiative properties. First, the report will explore documented applications of silica aerogel. Then, the chemistry and physics of sol-gel processing will introduce the theory section, followed by the microstructure of aerogel and its implications. After, the need for a valid optical model is expressed and the radiative transfer equation (RTE), its supporting equations, and boundary conditions are evaluated with respect to its application to porous, optically transparent materials. Methods in which PVPMS aerogel was synthesized and in which optical modelling was performed on TMOS aerogel will follow theoretical discussion. Finally, results of synthesis and modelling will be analyzed and discussed to close the report.

Applications

Silica aerogel's optical transparency, porosity, and low thermal conductivity make it an excellent material to use in a hybrid electric and thermal solar receiver [4]. The design proposed by Weinstein et al. uses aerogel to convert direct sunlight to both electricity and high-temperature thermal energy. Because silica aerogel exhibits high temperature stability (stable performance at 400-800^{o}C) [5], it can be used in a hybrid solar-thermal device to reduce thermal losses. This hybrid device collects solar radiation and converts it to high-temperature thermal energy, then the thermal energy is converted to electricity [4] [6]. This device is superior to traditional photovoltaics (PV) in that it is able to utilize the entire solar spectrum, not just a small range of it. The collected solar-thermal energy can be stored inexpensively using the aerogel which allows for the generation of electricity during overcast weather days [4].

Similarly, silica aerogel's optical transparency, low density, and low thermal conductivity can be applied to transparent insulation materials [7]. When evaluating a building's thermal envelope, it was found that windows are the weakest point in the envelope [8]. This is because traditional glazing systems consisting of panes of float glass filled with air have U-values up to 2.8 W/m^2-K [8], so a substantial amount of energy used to heat or cool a room can escape through a somewhat thermally conductive window. Buratti et al. propose that using transparent insulating materials—such as silica aerogel—in windows could satisfy visual comfort and energy efficiency with respect to heating and cooling of the building [8] [9] [10]. Glazing systems constructed by Buratti et al. with monolithic aerogel sandwiched between two panes of float glass demonstrated U-values as low as 0.6 W/m^2-K and transmittance as high as 81% [8]. This study determined that although the scattering effect produced by the aerogel decreased the

optical quality of vision, the diffusion of light significantly improves visual comfort by reducing glare [8].

Because of its low density and high porosity, silica aerogel can be used as a gas storage medium, specifically in space vehicles for rocket fuel storage [11]. The high porosity of the material allows how a high specific surface area, making silica aerogel an excellent candidate for heterogeneous catalysis, such as in the synthesis of nitrile from hydrocarbons using nitrogen oxide [11]. Other applications of silica aerogel regarding its low density and high porosity include fuel storage, ion exchange, and filters for gaseous pollutants [11].

Theory

Sol-Gel Processing

Generally, aerogel formation is thought to occur in three stages: polymerization of the monomer to form particles, growth of particles, and finally linking of particles into chains, then networks that extend throughout the liquid medium, thickening it to a gel [12]. However, this is an over-simplified version of all the chemical and physical processes that occur over the course of aerogel synthesis. More specifically, synthesis of silica aerogel follows the traditional sol-gel process of preparing the precursor, hydrolysis, condensation, gelation, aging, and drying [12]. First, the precursor solution should be prepared. The precursor should contain Si atoms bonded to a certain number of alkoxy substituent groups (-OR). The number of alkoxy groups surrounding the Si determine the number of siloxane bonds (Si-O-Si) in the final product. Siloxane bonds form the foundation of the thin solid backbone within the microstructure of aerogel. Thus, the number of alkoxy groups present in the initial precursor solution dictates the internal cross-linking density of the resulting aerogel. This property is important depending on

the desired results because it has been found that decreasing the cross-linking density can lead to increased transparency of the resulting aerogel [13]. However, not all cross-links are siloxane bonds; it is possible to introduce organic cross-linkers as well. Introducing organic cross-linking bonds may improve the mechanical strength of the aerogel against deformations by increasing the distance between Si atoms, further decreasing cross-linking density [13].

Once the precursor solution has been prepared, it is then hydrolyzed and condensed. It is common to combine hydrolysis and condensation into one step, although it is possible to execute the two reactions separately [13] [14] [15]. In the hydrolysis reaction, the general goal is to replace the alkoxy groups surrounding the Si atom with hydroxyl groups. A silicon alkoxide molecule reacts with water such that the hydroxyl group in the water molecule replaces the alkoxy group on the Si atom. The remaining negatively charged alkoxy group, ^{-}OR attracts the remaining hydrogen, H^{+} from water, forming an alcohol, ROH. This reaction is shown below in Equation 1 [12].

$$\equiv Si - OR + H - OH \leftrightarrow HO - Si \equiv + ROH \quad (1)$$

Hydrolysis can be either acid catalyzed or base catalyzed [12]. It may be necessary to use a homogenizing agent, such as an organic solvent or surfactant, during hydrolysis to prevent phase separation between nonpolar substituent groups (if present) and polar hydroxyl groups. Completed hydrolysis will yield silanol, $Si(OH)_4$. Regardless of the precursor used, hydrolysis will result in some or all of the alkoxy groups to be replaced by hydroxyl groups.

Following hydrolysis, a condensation reaction should be performed to yield siloxane bonds, forming the solid backbone of the aerogel's microstructure [12]. Siloxane bond formation by polycondensation can either occur by an alcohol producing condensation reaction, shown in Equation 2, or by a water producing condensation reaction, shown in Equation 3 [12].

$$\equiv Si - OR + HO - Si \equiv \leftrightarrow \equiv Si - O - Si \equiv + ROH \quad (2)$$

$$\equiv Si - OH + HO - Si \equiv \leftrightarrow \equiv Si - O - Si \equiv + H_2O \quad (3)$$

The alcohol producing condensation reaction shown in Equation 2 occurs when an alkoxy group and hydroxyl group collide, and the water producing condensation reaction shown in Equation 3 occurs when two hydroxyl groups collide.

Following the formation of siloxane bonds through polycondensation, the solution should be allowed to gel. During gelation, clusters form through further condensation of polymers and/or the aggregation of particles [12]. These clusters grow and collide with each other, the links form between the clusters to produce a single "parent" cluster. Thus, the gel has formed, and at this point, many smaller clusters are still present in the sol phase. The parent cluster branches throughout the sol phase and, with time, the smaller clusters attach themselves to the solid network, stiffening the gel [12].

Once the parent cluster has reached the limits of the container, having fully branched through and stiffened the sol phase, gelation gives way to the aging process. The aging process can generally be thought of as the progressive strengthening and stiffening of the gel [12]. Whenever the solid phase is at least partially soluble with the liquid phase, smaller clusters present in the solid phase can dissolve into the liquid phase and collide with other small clusters, thus linking together to form a larger cluster. This larger cluster can then reprecipitate back onto the parent cluster on surfaces of lower curvature [12]. Cyclic processes of dissolution and reprecipitation coarsens the solid backbone of the microstructure, as the dissolved clusters settle into the crevices of the spherical particle comprised backbone.

Aging of the gel is crucial to aerogel synthesis because the coarsening and strengthening that takes place allows the network to bear the capillary stresses exerted on the microstructure

during drying [16]. Depending on the extent and rigor of the aging process, over-coarsening the gel network may result in the reduction in specific surface area and the loss of pores which are integral to maintaining the superior optical and thermal properties of the material [12]. Manipulating the aging time and temperature may help control the coarsening effects of the microstructure to the desired effect. It has been found that specific surface area decreases with the degree of Ostwald ripening (the cluster dissolution and precipitation process occurring during aging) which increases with increasing aging time and temperature [16]. Furthermore, the type of solvent used to expedite the aging process also affects a myriad of physical properties of the wet gel such as specific surface area, hydrophobicity, and pore diameter [17].

After the aging process, a liquid phase (consisting of unreacted reagents and products of hydrolysis and condensation) is present in the pores of the wet gel. The goal of the drying process is to remove the liquid phase entirely. However, the low density of aerogel implies that the solid volume fraction is very low. Drying the alcogel must be done very carefully so as to preserve the fragile pore network. The interface between solid and vapor phases is far more energetic than a solid-liquid interface. Therefore, as the solvent is evaporated from the pores of the aerogel, the liquid covers the solid to reduce the energetic interface, effectively forming a meniscus within each pore [18]. With liquid solvent covering as much surface area within the pore as possible, the solid surfaces are pulled together as evaporation continues.

That being said, the first stage of drying--called the constant rate period, when the pores are filled with liquid--is the most significant to the integrity of the gel [18]. Here, the tensile forces of the liquid are supported by the normal forces exerted by the solid phase. Therefore, the solid phase goes into compression, causing it to contract into the liquid phase, while the liquid meniscus remains at the exterior surface [18]. As drying continues, the liquid meniscus deepens,

further increasing the tensile forces in the liquid. At the same time, the solid network stiffens as new bonds are forming and porosity decreases [18]. The constant rate period of drying comes to an end when the radius of the meniscus equals the radius of the pore, at which point the meniscus retreats into the pore, leaving it filled with air.

The most common method of drying aerogel is through supercritical drying, where the liquid in the pores is brought to the gaseous phase in the absence of surface tension and capillary stress. First, the aerogel sample with liquid solvent filling its pores is placed into a vessel suitable for large temperature and pressure variation. The vessel is then flushed with liquid CO_2 several times to replace the solvent-filled pores with liquid CO_2. Then, the vessel is heated and pressurized past the critical point of CO_2 such that it is transformed into its supercritical phase. When any liquid approaches its critical point, attractive forces between molecules become negligible, therefore decreasing the surface tension of the liquid as well as the capillary stress it can exert [19]. Thus, at its critical point, CO_2 is rid of all surface tension and ability to exert capillary stress on the fragile nanostructured pore network. With the pore network intact, the supercritical CO_2 can be removed by isothermally depressurizing the vessel, leaving the dried aerogel product.

However, supercritical drying of aerogel comes with several major disadvantages. First, reaching supercritical temperatures and pressure requires a significant amount of energy. Furthermore, constructing a vessel robust enough to withstand large temperature and pressure swings is expensive in raw materials alone. If such a vessel is not constructed correctly, the high pressure exerted can lead to explosion, thus compromising the safety of the laboratory and its personnel. Finally, the size of the aerogel sample that can be synthesized is limited to the

dimensions of the pressurized vessel. This size limitation can be inconvenient for applications requiring large aerogel samples, such as glazing systems and solar-thermal energy capture.

Replacing supercritical drying with ambient pressure drying can address cost and safety concerns associated with the former. Ambient pressure drying simply allows for the evaporation of the solvent within the pores of the wet gel at room temperature and pressure. This method is superior to supercritical drying in terms of cost savings and safety maintenance. However, the rate of diffusion of air onto the sample and the rate of solvent evaporation must be carefully controlled, and this can be difficult to do. If solvent evaporation from the sample occurs too quickly, the capillary stresses exerted on the fragile backbone can be overwhelming, causing the pore structure to collapse, effectively ruining the transparency of the sample.

Overall, the process of sol-gel synthesis can be summarized below in the schematic shown in Figure 1.

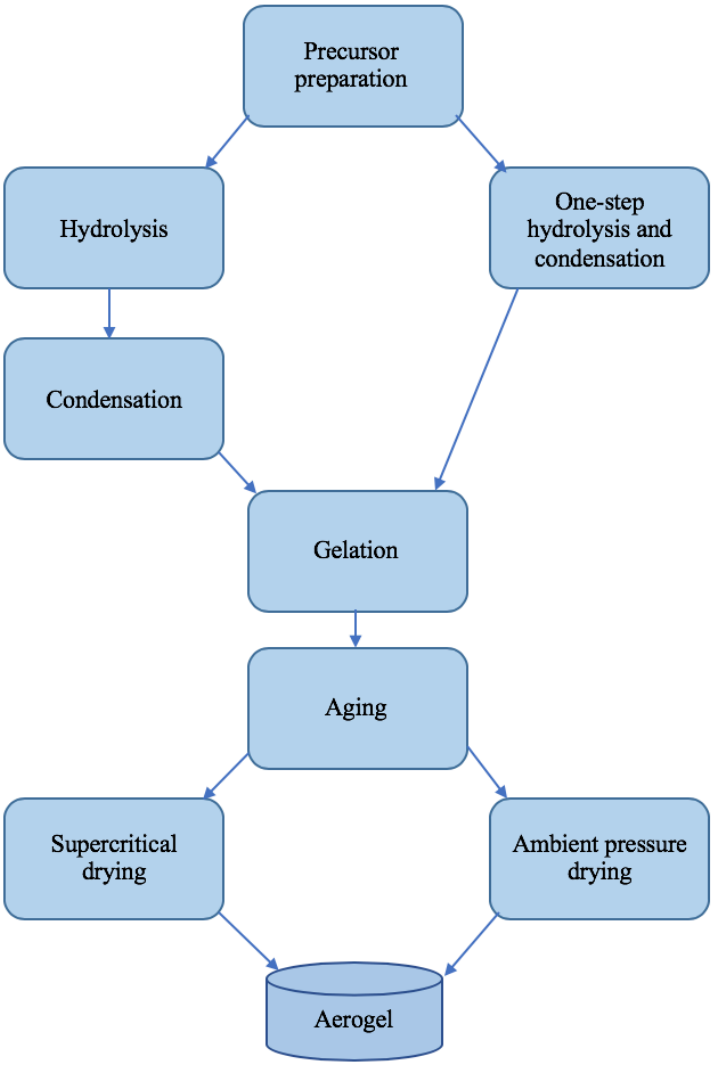

Figure 1: Sol-Gel Processing Schematic Diagram

Aerogel Microstructure

The microstructure of silica aerogel consists primarily of two components: air-filled pores, and a thin solid backbone encapsulating the pores. The backbone is composed of approximately spherical silica particles which are strung together with siloxane bonds, appearing similar to threaded pearls on a string. Because multiple siloxane bonds can be present for any one Si atom, cross-links form, creating a three dimensional pore network. A field emission

scanning electron microscope (FESEM) image collected by Zu et al. shows the microstructure of silica aerogel [14], and Figure 2 shows this along with a schematic representation of the microstructure to show its two components.

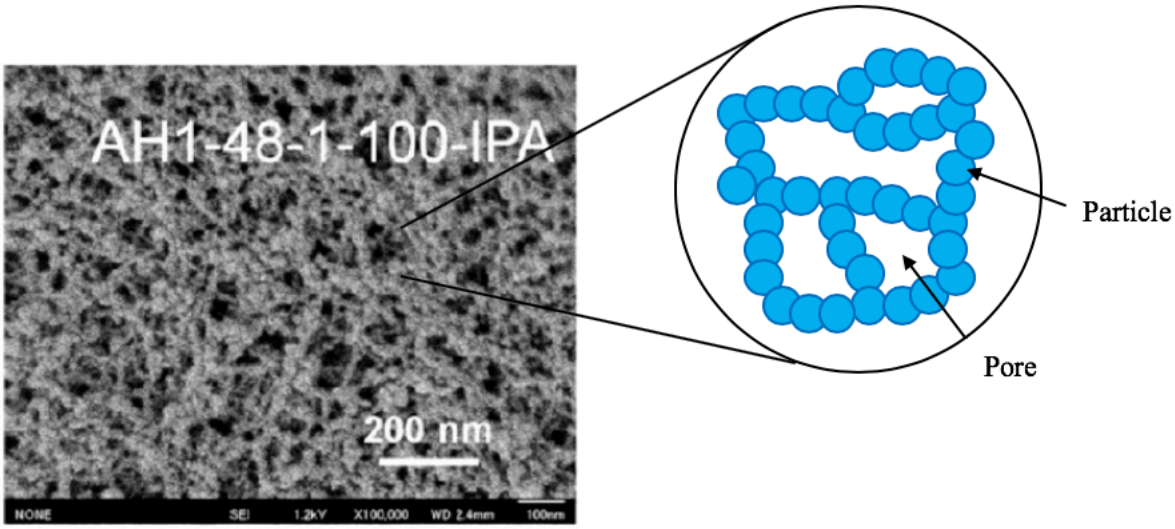

Figure 2: Aerogel Microstructure Schematic from FESEM Image *[14]*

The silica particle diameter is typically larger than the pore diameter, often ranging between 7 nm and 200 nm [15] [20]. That being said, the average diameter of silica aerogel pores ranges from 5 nm to 35 nm [15] [20]. It is important to know the uniformity of the pore network within a sample, since a smaller pore size distribution is typically associated with higher transparency. Moreover, light scattering effects can be reduced with smaller pores and particles so long as the distribution in size is uniform. In fact, it was found that reduced transparency of aerogel systems was the result of large particle and cluster sizes [21].

As shown in the FESEM image in Figure 2, the thin solid backbone constitutes a low solid volume fraction. This low solid volume fraction combined with high porosity explains the low density of the material. Aerogel's microstructure can also be used to explain its optical

transparency. Both the pores and particles constituting the microstructure are responsible for the scattering of incident light. However, since the average pore and particle size are smaller than the wavelengths comprising the visible light range, scattering effects are significantly reduced, lending a transparent sample. Moreover, the mass specific extinction for aerogels was found to be a function of the sample's density, thickness, and wavelength measured [22]. So, at any given density, the particle diameter must be kept small to reduce light extinction [21].

Thermally insulating properties of silica aerogel also arise from the delicate microstructure, as it suppresses all three modes of heat transfer. The low solid volume fraction and thus low density of the material both imply that heat transfer through conduction is negligible. Convective heat transfer is also depressed because the average pore diameter is smaller than the mean free path of air. With respect to radiative heat transfer, silica aerogel absorbs thermal energy in the infrared region [5]. This thermal energy absorption creates a greenhouse effect within the material, effectively preventing radiative heat loss.

Optical Modeling

Because optical transparency in silica aerogel is crucial for solar-thermal and glazing system applications, it is necessary to develop an accurate and cohesive model describing the mesoporous material's optical performance [7] [8] [10] [15]. Silica aerogel's microstructure is largely attributed to its ability to transmit light, since the particles and pores that constitute it act as Rayleigh scattering centers [21] [24]. The Rayleigh-Gans scattering phenomenon occurs within small, near-dielectric spheres wherein the light phase velocity inside the particle is less than it is outside the particle. Therefore, light traveling through the particle (or aerogel sample) will exhibit phase lag compared to incident light outside the sample [25]. Rayleigh scattering is

essentially elastic, meaning that the frequency of the scattered light is equal to the frequency of the incident radiation [26]. The schematic in Figure 3 below shows the effect of a Rayleigh scattering center on incident light.

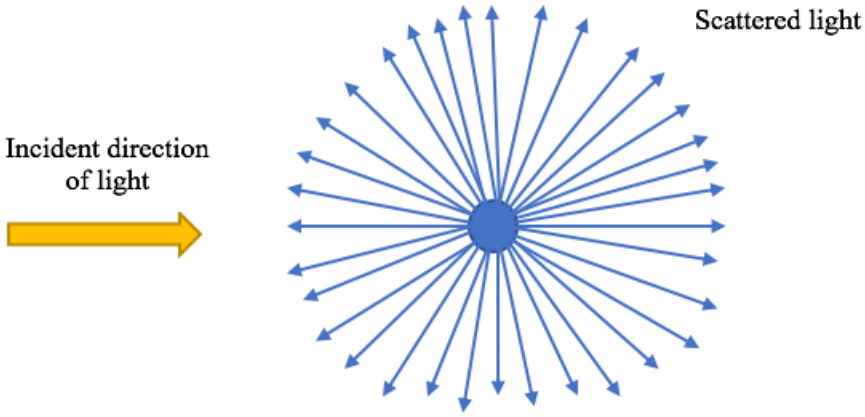

Figure 3: Rayleigh Scattering Center

Since both aerogel pores and its particles act as Rayleigh scattering centers, incoming light is scattered hundreds of times before ever emerging from the sample. The multiple scattering effect describes the phenomenon in which photons are scattered from the samples and then scattered again by neighboring particles prior to reaching an instrument's light detector. Therefore, it can be concluded that silica aerogel is a multiple scattering medium.

In 1998, Arlon J. Hunt proposed that within the visible light region, the transmittance of aerogel could be well modelled by Equation 4 [15] [27].

$$T = A \times \exp\left(\frac{Bt}{\lambda^4}\right) \quad (4)$$

The parameter A in Hunt's model represents a wavelength independent coefficient accounting for scattering from surface damage, channels arising from solvent flow, and cracks. B describes the extinction coefficient and is wavelength dependent, and t is the thickness of the

sample. Equation 4 was developed by Hunt to compare the transparency of aerogel samples with various thicknesses, origins, and surface conditions in order to separate intrinsic and extrinsic qualities of the samples [27].

However, there are a few problems with using Hunt's equation to model aerogel transmission. For one, Hunt's extinction coefficient, B, only accounts for scattering, so the model cannot be used in regions of the light spectrum where absorption is present [15]. Secondly, Hunt's model can be inaccurate in regions of the light spectrum where scattering is dominant [15]. This is because Equation 4 is based on the Beer-Lambert (B-L) law, which only focuses on a single light propagation direction. As we have seen, silica aerogel is a highly multiple scattering medium, therefore all propagation directions must be coupled to account for this [15] [27] [25]. That being said, Equation 4 can also be inaccurate when modeling hemispherical flux, which is comprised of both direct and diffuse, as opposed to directional flux. Since the present work is interested in modelling hemispherical transmittance and reflectance, Hunt's model will not be used due to its inaccuracies.

Radiative Transfer Equation

The radiative transfer equation (RTE), as opposed to Hunt's model, describes the intensity of incident and scattered light as a function of the light's angle and position within the medium. Thus, the RTE captures the multi-directional nature of the problem of interest. In fact, the RTE has been in various studies to investigate silica aerogel's radiative properties in the infrared region of the light spectrum, which were found to have significant effects on the material's thermal insulating properties [28] [29]. If the RTE is valid in scattering-dominant regions of the light spectrum (visible wavelengths and smaller) as well as the infrared region, this

implies that the model is versatile and can be used accurately over a broad range of wavelengths. If this is the case, it is possible to fully capture silica aerogel's optical performance over the scattering dominant region as well as the absorption dominant region. This way, it is possible to decouple extinction contributions from both scattering and absorption and better understand more broadly the optical performance of aerogel.

Before delving into the RTE, it would be useful to define the variables that give sustenance to the model. First, the extinction coefficient, denoted as β, describes the degree to which light is attenuated—or not transmitted—through the material as light propagates within it. In this study, one goal is to decouple light extinction into scattering contributions by defining the scattering coefficient (σ_s) and absorption contributions by defining the absorption coefficient (σ_a). Optical thickness, or ξ, describes light attenuation as a function of the sample thickness. The scattering albedo represents the ratio of scattered light to all attenuated light and is denoted by ω. Lastly, the cosine of the polar angle of scattered light with respect to the incident light's direction is represented by $\mu = \cos(\theta)$.

The 1-D azimuthal radiative transfer equation that describes wavelength dependent light intensity as a function of angle and spatial distance is shown below in Equation 5 [15] [25].

$$\mu \frac{\partial I_\lambda(\xi_\lambda,\mu)}{\partial \xi_\lambda} = -I_\lambda(\xi_\lambda,\mu) + \frac{\omega_\lambda}{2}\int_{-1}^{1} I_\lambda(\xi_\lambda,\mu')d\mu' \quad (5)$$

If the first term on the right-hand side of Equation 5 is added to both sides of the equation, the result is shown in Equation 6.

$$\mu \frac{\partial I_\lambda(\xi_\lambda,\mu)}{\partial \xi_\lambda} + I_\lambda(\xi_\lambda,\mu) = \frac{\omega_\lambda}{2}\int_{-1}^{1} I_\lambda(\xi_\lambda,\mu')d\mu' \quad (6)$$

Equation 6 describes that the hemispherical sum of the scattered light intensity (integral term of the left-hand side) is equal to the sum of the incident light plus the rate of change of light intensity with respect to spatial position within the medium corrected by the directional term, μ.

Written in this form, the RTE neglects thermal emission nanoscale particle scattering is assumed to be isotropic, which is known as the transport approximation [15] [25]. It is important to note that quantities in Equation 5 that have subscript λ are wavelength dependent quantities. That being said, optical thickness can be calculated by multiplying the extinction coefficient by the physical thickness of the aerogel sample, x, as shown in Equation 7.

$$\xi_\lambda = \beta_\lambda x \tag{7}$$

The scattering albedo can be determined by dividing the scattering coefficient by the extinction coefficient, as represented by Equation 8.

$$\omega_\lambda = {}^{\sigma_s}/_{\beta_\lambda} \tag{8}$$

Coefficients of scattering and absorption can be determined from the scattering albedo and extinction coefficient using Equations 9 and 10, as shown below.

$$\sigma_s = \omega_\lambda \beta_\lambda \tag{9}$$

$$\sigma_a = (1 - \omega_\lambda)\beta_\lambda \tag{10}$$

The relative refractive index of silica aerogel is close to 1, so the boundary conditions used to solve Equation 5 at x = 0 and x = t are given below.

$$\begin{cases} I_\lambda(0,\mu) = \Phi, \text{if } \mu_0 \le \mu \le 1 \\ I_\lambda(0,\mu) = 0, \text{if } 0 \le \mu \le \mu_0 \end{cases}$$

$$I_\lambda(\xi(x = t), \mu) = 0 \text{ for } \mu \le 0$$

The first boundary condition at x = 0 describes the condition of the light as it first comes into contact with the aerogel slab. It shows that the intensity of the light as it first hits the sample is equal to the incident flux if light hits the sample at the same angle as the incident light angle. At any other angle, the light intensity is equal to zero, shown by the second boundary condition at x = 0. The last boundary condition says that at the last boundary—after the light has traveled

through the entire sample and is exiting the sample—the intensity of light is equal to zero if the light's angle is between 90° and 270°.

A schematic showing the angular nature of light transmitted through and reflected from an aerogel sample is shown below in Figure 4.

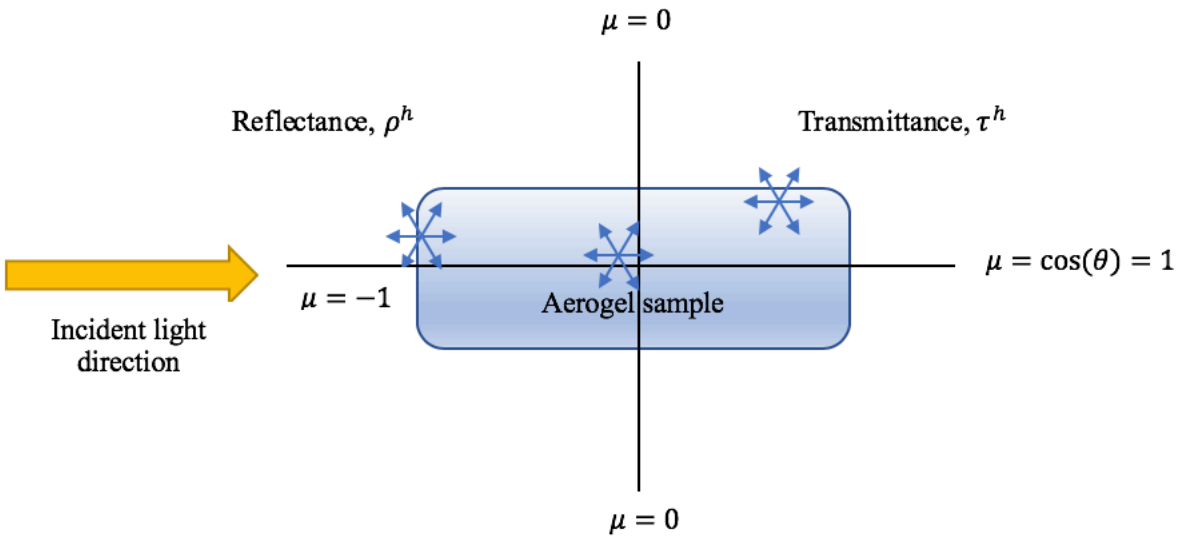

Figure 4: Angular Dependence of Transmitted and Reflected Light

Up to this point, the goal is to solve the RTE for the intensity field of light, I_λ. It follows that once the field of intensity of scattered light is known, the hemispherical transmittance can be calculated by taking the directional sum from $\mu = 0$ (90° vertical) to $\mu = 1$ at the second boundary, $\xi(x = t)$. In essence, hemispherical transmittance is calculated as the sum of all light that is scattered into the first quadrant of the cartesian plane, or the forward direction, as shown in Equation 11 [15].

$$\tau^h = \frac{\int_0^1 I_\lambda(\xi(x=t),\mu)\mu d\mu}{\int_{\mu_0}^1 \Phi\mu d\mu} \tag{11}$$

It is important to note that in Equation 10, the directional sum of the transmitted light intensity is normalized by the incident flux which—in the simplest case—is equal to 1.

In a similar fashion, the hemispherical reflectance can be calculated as the directional sum from the vertical ($\mu = 0$) to the horizontal at 180°, or $\mu = -1$ at the first boundary when $\xi(x = 0)$. In this way, the hemispherical reflectance represents the sum of all light that is scattered backward into the second quadrant of the cartesian plane—or the backward direction—and then normalized by the incident flux, as shown in Equation 12.

$$\rho^h = \frac{-\int_{-1}^{0} I_\lambda(\xi(x=0),\mu)\mu d\mu}{\int_{\mu_0}^{1} \Phi\mu d\mu} \tag{12}$$

To better understand the inherent scattering properties of the material, it is useful to find the distribution of the effective scattering center diameter over a broad spectrum of wavelengths. Conveniently, the effective scattering center diameter model of a mesoporous medium like silica aerogel coincides with the Rayleigh-Gans theory [15] [24]. The Rayleigh-Gans theory relates the scattering center diameter to the scattering coefficient—which can be found using the RTE model—and other known quantities such as the apparent density of the aerogel sample and its relative refractive index, as shown in Equation 13 [15].

$$\sigma_s = 4\pi^4 \frac{\rho_{ap}}{\rho_{SiO2}} \frac{d^3}{\lambda^4} \left(\frac{n^2-1}{n^2+2}\right) \tag{13}$$

TMOS Aerogel

TMOS (tetramethyl orthosilicate) aerogel is one of the most common and widely used types of aerogel. A research team at Massachusetts Institute of Technology developed a rapid one-step hydrolysis-condensation procedure to yield transparent and ultra-low density TMOS aerogel [30]. The synthesis begins with the preparation of the precursor solution which contains

TMOS ($Si(OCH_3)_4$), methanol, water, and ammonium hydroxide (NH_4OH). Once a container is charged with the precursor solution, it is left to gel at ambient pressure and temperature. During the gelation process, the mild basic catalyst aids in the removal of CH_3 and is replaced with a proton from water. The remaining hydroxyl group with water bonds with the positively charged methyl ion to form methanol. Subsequent condensation yields a gel consisting mostly of siloxane bonds ($\equiv Si - O - Si \equiv$).

Gelation proceeds quickly, taking only 30 minutes in total at ambient conditions [30]. It was found in the study that the optimal base catalyst ratio ($3.5(10^{-2})$ mol NH_4OH : mol TMOS) balances the rates of hydrolysis and condensation reactions, allowing for a short gelation time. This delicate balance enables rapid growth of the silica particles and an abrupt ending of growth due to the depleted presence of precursor [30]. Such a rapid reaction yields a highly uniform porous structure with a smaller particle size which effectively reduces the degree of light scattering which increases the transmittance of the resulting sample.

Once the precursor has gelled, it is washed in an ethanol bath to remove any residual chemicals at ambient conditions. The wet gel is then dried using the supercritical drying method after ethanol solvent exchanges. This method of TMOS aerogel preparation has been shown to yield highly transparent samples with solar weighted transmittance of 94.8% at a thickness of 10 mm [30].

PVPMS Aerogel Synthesis

The present work reports the synthesis of polyvinylpolymethylsiloxane (PVPMS, $(CH_2CH(Si(CH_3)O_{2/2}))_n$) aerogel, first proposed by Zu et al [14]. PVPMS is prepared using a difunctional precursor which contains a methyl group, a vinyl group, and two alkoxy groups.

Both the vinyl group and two alkoxy groups provide potential cross-linking sites, allowing two cross-linked networks to form. The flexible, aliphatic hydrocarbon chains making up one of the cross-linked networks are able to fold and stretch without fracturing material [14]. The doubly cross-linked structure of PVPMS aerogel mechanically reinforces the material against bending and compression without compromising optical transparency and leads to a combination of low density, high specific surface area, hydrophobicity, and thermally insulating properties [14].

First, the difunctional precursor, vinylmethyldiemthoxysilane (VMDMS) undergoes radical polymerization by di-*tert*-butyl peroxide (1 or 5 mol%) to yield polyvinylmethyldimethoxysilane (PVMDMS). To prepare the solution, one should add 0.889 g of VMDMS to a glass vial, and then add 0.0727 g of DTBP to the VMDMS.

Before the precursor is radically polymerized, it only contains two hydrolysable groups and would not form a 3-D cross-linked structure alone [14]. After radical polymerization, it becomes difunctional, allowing the desired doubly cross-linked structure to form. The performance of this step will determine the quality of the resulting aerogel or xerogel. This is because the precursor solution must be prepared under vacuum and flushed with argon gas [14] to prevent oxygen contamination in the radical polymerization process. In our case, a glove box equipped with a vacuum pump and argon flushing system is used. During polymerization oxygen can form an alternate copolymer—a polyperoxide—in a reaction that competes with the typical radical propagation, thus inhibiting the desired polymerization [31]. At about 100-150ºC, the polyperoxides may decompose into free radicals that can reinitiate polymerization [31]. Thus, it was found that when radical polymerization is executed and only traces of oxygen are present, an induction period is always observed to slow or halt the radical polymerization process [31].

After the precursor solution is prepared in a glass vial under vacuum, the vial should be taped with a heat-resistant material—this method uses Teflon tape—and placed inside a hydrothermal reactor. The hydrothermal reactor should be placed in a 120^{o}C oven for 24-48 hours. Successful polymerization should yield a transparent, colorless, and highly viscous solution. Further synthesis steps should be executed only after verifying that polymerization has occurred without oxygen contamination. Physical signs of and oxygen contaminated sample include a yellow tint, lost sample volume, and premature sample solidification. If any of these physical indicators are observed, no further synthesis steps should be performed on the sample.

Once the solution is as viscous as possible without solidifying, one-step hydrolysis and condensation can be executed on the sample. To do this, add to a separate vial 3.126 g of benzyl alcohol (BzOH), then 0.187 g of water, and finally 0.0735 g of tetramethylammonium hydroxide (TMAOH). These amounts will result in the following molar ratios: 4.3 mol BzOH: mol Si, 2 mol H_2O: mol Si, and 0.03 mol TMAOH: mol Si [14]. The water is used as the primary agent of hydrolysis and TMAOH is used to catalyze the reaction. BzOH is added to suppress macroscopic phase separation within the solution, as it contains both a nonpolar benzyl substituent group as well as a polar hydroxyl group. Addition of BzOH to the solution is absolutely necessary because the resulting solution contains a combination of hydroxyl groups, siloxane bonds, methyl groups, and aliphatic hydrocarbon chains. If a homogenizing agent is not added, the differences in polarity will induce phase separation. If the phases are allowed to separate, a homogenous pore structure will be unable to form, and will ruin the transparency of the resulting sample.

Once the mixture of BzOH, water, and TMAOH is prepared, it should be transferred to the room-temperature, viscous precursor solution using a pipette. Once combined, the gelation solution needs to be thoroughly mixed. This can be done by loading the glass vial into a

mechanical stirrer, and then stirring the solution for 5-10 minutes. After the solution has been mixed, it will be ready to undergo gelation and aging.

The solution should be gelled at 80°C for 1 hour in the glass vial. After 1 hour, the glass vial is to be transferred to an oven at 100°C where it will be left to age for 4 days. Once aging is complete, the gelled sample will need to be removed from its glass vial to undergo 3 rounds of solvent exchanging using a low-surface tension solvent. Solvent exchanging is performed to remove residual chemicals and unwanted reaction by-products [17] [12] [18]. For this experiment, the wet gel was placed in an isopropyl alcohol (IPA) bath to undergo solvent exchange at 60°C overnight. This was repeated for a total of 3 solvent exchanges.

After the solvent exchanging process is complete, the alcogel is ready to be dried. This experiment uses the ambient pressure drying method as opposed to the supercritical drying method. Ambient pressure drying is performed using the pin-hole drying method. The alcogels are transferred from their solvent into a small petri dish. The petri dish is to have a small, pin-sized hole poked into the lid. Then, the petri dish containing the aerogel sample is taped with Teflon tape to avoid air leaks. This way, the rate of air diffusion onto the wet gel is inhibited in a way that the solvent cannot evaporate from the sample too quickly. This is done to reduce capillary stresses on the sample and thus increase the transparency of the dried sample. The aerogel-like xerogels will be completely dried after 3-4 weeks of being in the petri dish.

Optical Modeling Methods

Radiative Transfer Equation Solution

The first step in modeling the optical properties of silica aerogel is to solve the radiative transfer equation as it is written in Equation 5 for the intensity field of light, or $I_\lambda(\xi_\lambda, \mu)$. Since

the intensity of light in this equation is a function of optical thickness as well as the cosine of the polar angle, both spatial position and angle must be discretized using the discrete ordinate method (DOM). The length, or spatial position, will be discretized as $k = 1, \dots, N_k$ and angle will be discretized as $i = \pm 1, \dots, \pm N_i$. Note that the +/- sign associated with discretized angle is used to include all angles of the hemisphere, as $\mu = \cos(\theta)$ will be negative in the second quadrant of the cartesian coordinate system, and the second quadrant will later be used to calculate hemispherical reflectance. $I_\lambda(\xi_\lambda, \mu)$ can thus be denoted as $I(\xi_k, \mu_i)$.

The integral portion of the RTE can readily be simplified using Gaussian quadrature as follows:

$$\int_{-1}^{1} I(\xi_k, \mu')d\mu' \approx \sum_{i=-N_i}^{i=N_i(i\neq 0)} w_i I(\xi_k, \mu_i) \tag{14}$$

Gaussian quadrature is a method of approximating a definite integral as the weighted sum of the function at specific points that are inside the domain of integration. In this case, the specified function values will be the nodes set by discretizing position and angle, and the Gauss weights at these points, w_i have already been documented.

It is desirable to have intensity values in the middle of each position node (k+1/2), as an average of, say, node 1 and node 2. When rewriting the position discretization, the angle should be held constant. This should be written as:

$$I(\xi_{k+\frac{1}{2}}, \mu_i) \approx \frac{1}{2}[I(\xi_k, \mu_i) + I(\xi_{k+1}, \mu_i)] \tag{15}$$

Now, Equation 5 can be rewritten by accounting for discretized position and angle, where for simplicity $I(\xi_k, \mu_i) = I_k^i$. The discretized RTE is shown below in Equation 16.

$$\mu_i \frac{I_{k+1}^i - I_k^i}{\Delta x} = -I_{k+\frac{1}{2}}^i + \frac{\omega}{2}\sum_{j=-N_i}^{j=N_i} w_j I_{k+\frac{1}{2}}^i \tag{16}$$

Equations 15 and 16 can be combined for inserting the expression for $I^i_{k+1/2}$ into Equation 16:

$$\mu_i \frac{I^i_{k+1} - I^i_k}{\Delta x} = -\frac{1}{2}\left(I^i_k + I^i_{k+1}\right) + \frac{\omega}{4}\sum w_j (I^i_k + I^i_{k+1}) \tag{17}$$

Equation 17 can further be reorganized as:

$$\left(\frac{\mu_i}{\Delta x} + \frac{1}{2}\right) I^i_{k+1} = \left(\frac{\mu_i}{\Delta x} - \frac{1}{2}\right) I^i_k + \frac{\omega}{4}\sum w_j (I^i_k + I^i_{k+1}) \tag{18}$$

Now, it is possible to rewrite Equation 18 to solve for I^i_{k+1}, the intensity at the next position over from I^i_k.

$$I^i_{k+1} = \frac{\left(\frac{\mu_i}{\Delta x} - \frac{1}{2}\right)}{\left(\frac{\mu_i}{\Delta x} + \frac{1}{2}\right)} I^i_k + \frac{\omega/4}{\left(\frac{\mu_i}{\Delta x} + \frac{1}{2}\right)} \sum w_j \, (I^i_k + I^i_{k+1}) \tag{19}$$

For simplicity, we will set $\alpha^i = \frac{\left(\frac{\mu_i}{\Delta x} - \frac{1}{2}\right)}{\left(\frac{\mu_i}{\Delta x} + \frac{1}{2}\right)}$ and $\gamma^i = \frac{\omega/4}{\left(\frac{\mu_i}{\Delta x} + \frac{1}{2}\right)}$. Substituting these values into Equation 19 and distributing γ^i over the summation term leads to Equation 20.

$$I^i_{k+1} = \alpha^i I^i_k + \gamma^i \sum w_j I^i_k + \gamma^i \sum w_j I^i_{k+1} \tag{20}$$

The objective of the previous and following manipulations to the original radiative transfer equation is to calculate the value of the intensity of light at each subsequent discretized position. If the incident light intensity is known, that is, the intensity of light just before it hits the aerogel sample, I_k^i, then it will be possible to use that value of intensity to calculate the next intensity value after it has penetrated the sample, or I_{k+1}^i, based on the predictions of the RTE.

This method of solving the RTE is executed computationally using the computing software Python, and it is desired to avoid using loops, as loops often take more time to run and more computing power. Therefore, Equation 20 must be manipulated in such a way to calculate the intensity field of scattered light, I_{k+1}^i using matrix algebra.

From Equation 20, if the coefficients of the variables of I_k an I_{k+1} are separated and combined, it can be re-expressed as Equation 21, where I represents the identity matrix $\begin{bmatrix} 1 & \cdots & 0 \\ \vdots & \ddots & \vdots \\ 0 & \cdots & 1 \end{bmatrix}$.

$$\left(I - \gamma^i \sum w_j\right) I_{k+1}^i = (\alpha^i + \gamma^i \sum w_j) I_k^i \tag{21}$$

Because the expression represented by α is a function of both discretized length and angle, its matrix denotation will be $[C_{ij}]$. This way, it will be a 2 dimensional vector that accounts for every discretized position and every discretized angle. Similarly $[B_{ij}]$ will represent the $\gamma^i \sum w_j$ term on the left-hand side of Equation 21, and $[D_{ij}]$ will be set equal to the $\gamma^i \sum w_j$ term on the right-hand side of Equation 21.

With this in mind, Equation 21 can be expressed in matrix form using Equation 22 below.

$$\left[I - B_{ij}\right]\left[I_{k+1}^i\right] = \left[C_{ij} + D_{ij}\right]\left[I_k^i\right] \tag{22}$$

While fixing the position, the angle can be varied, thus $[I_{k+1}] = \begin{bmatrix} I_{k+1}^{-N_i} \\ I_{k+1}^{-N_i+1} \\ \cdots \\ I_{k+1}^{1} \\ \cdots \\ I_{k+1}^{N_i} \end{bmatrix}$.

Finally, $\left[I_{k+1}^i\right]$ can be calculated from the incident intensity field of light using Equation 23.

$$\left[I_{k+1}^i\right] = [I - B_{ij}]^{-1} \cdot [C_{ij} + D_{ij}][I_k^i] \tag{23}$$

Therefore, by using arbitrary values of ξ (constituting the length discretization), μ (constituting the angle discretization), and ω (which will be varied from 0 to 1 since it is a ratio), it is possible to calculate the intensity of light as a result of passing through an aerogel sample from the incident intensity of light.

From the intensity field predicted by the RTE model, it is possible to then calculate hemispherical transmittance and reflectance using Equations 11 and 12.

Finding Inherent Optical Properties from Experimental Data

Once the hemispherical transmittance and reflectance are calculated from the predicted intensity field modelled by the radiative transfer equation, both quantities can be considered to be functions of both scattering albedo and optical thickness. This is true because the modelled intensity was calculated from arbitrary values of scattering albedo and optical thickness, and hemispherical transmittance and reflectance are calculated from the same intensity field. Therefore, two separate plots of scattering albedo versus optical thickness can be created with the contour map of both hemispherical transmittance and reflectance overlaid as the third axis. These plots will thus define how both transmittance and reflectance of an aerogel sample change with their inherent values of scattering albedo and optical thickness at each wavelength.

These plots—which will be presented in the results section of this report—will be used as the basis of finding the inherent optical properties of TMOS aerogel prepared by an MIT lab. First, the data from the two plots will be condensed into separate transmittance and reflectance maps. These maps will contain every value of transmittance and reflectance for every combination of (ω, ξ) as modelled by the RTE. Here, ω varies from 0 to 1 and ξ varies from 0 to 5. Then, experimental transmittance and reflectance data will be collected from the TMOS aerogel sample using a UV-vis-NIR spectrophotometer across a broad range of wavelengths (250 nm to 2500 nm) in order to investigate extinction contributions from both scattering and absorption. The objective in this is to compare the experimentally collected transmittance and

reflectance data the transmittance and reflectance spectra modelled by the RTE as functions of scattering albedo and optical thickness.

For example, if a certain aerogel sample A has a transmittance value of 80% at 550 nm and a reflectance value of 15% at 550 nm, these two values would represent one contour level on each of the contour plots constructed as mentioned before. So, a contour line of 80% can be specified on the transmittance contour plot and a contour line of 15% can be specified on the reflectance contour plot. Since both contour plots of transmittance and reflectance use the same axis bounds and intervals (values of scattering albedo and optical thickness), these two contour lines can be superimposed onto one another on the same plot. When this is done, the two contour lines will have exactly one intersection, and this intersection provides a y-value and an x-value. The exact location of the one intersection between the two contour lines at the specified wavelength thus yields a value of scattering albedo and optical thickness. The extinction coefficient, β can easily be found from the value of optical thickness provided by the location of the intersection by dividing it by the physical thickness of the aerogel sample.

The process described above needs to be repeated for all values of transmittance and reflectance as the example describes the intersection of transmittance and reflectance at one specific wavelengths. However, it is desired to derive the inherent optical properties of our samples for all wavelengths collected by the UV-vis-NIR apparatus. To get all intersection values for the experimentally collected transmittance and reflectance data, first a contour plot of the RTE-modelled transmittance against scattering albedo and optical thickness must be constructed, just as before, only this time, the levels on the contour plot are set as the experimental values of transmittance. Then, the data within the contour lines are collected and stored, and the x-values are defined as values of scattering albedo, and the y-values are stored as

values of optical thickness. Next, the all intersections in this collection of data are found using a GitHub's Sukhbinder intersection function [32]. The intersection data is stored in a two-dimensional array containing intersection values of scattering albedo and optical thickness. The values of scattering albedo and optical thickness can then be stored in two separate lists.

Once the values of scattering albedo and optical thickness are found for all intersections of experimental transmittance and reflectance for a particular sample, both values can be plotted against wavelength. In this way, it will be possible to investigate the total attenuative properties of a particular aerogel sample over a broad range of wavelengths. Furthermore, using the calculate values of scattering albedo, optical thickness, and physical thickness of the sample, the coefficients of scattering and absorption (σ_s and σ_a) can be determined for all wavelengths using Equations 7, 9, and 10. When the coefficients of scattering and absorption are plotted against wavelength, it will be possible to examine a sample's extinction contributions from scattering and absorption separately, which will give insight into the inherent optical properties of that specific sample.

Now with the scattering coefficient known over all wavelengths for which data was collected, all variables necessary to calculate the effective scattering center diameter using Equation 13 are known. Equation 13 can be rearranged to solve for the effective scattering center diameter, d_{sc} as shown in Equation 24.

$$d_{sc} = \sqrt[3]{\lambda^4 \left(\frac{\sigma_s}{4\pi^4}\right)\left(\frac{\rho_{SiO2}}{\rho_{app}}\right)\left(\frac{n^2+2}{n^2-1}\right)} \tag{24}$$

Finally, the scattering center diameter of a particular sample can be can be plotted against wavelength.

Results and Discussion

PVPMS Aerogel Transmittance

The experimental trials of this study were successful in synthesizing ambient-dried PVPMS aerogel monoliths. To begin the discussion of PVPMS aerogel synthesis results, this section of the report will compare 9 samples with slightly different synthesis techniques. The transmittance of these samples has been adjusted such that their transmittance spectra reflect having thicknesses of 2.2 mm. Since transmittance is altered by the optical thickness of each sample—which is a function of the physical thickness of a sample—the transmittance was adjusted so that the thicknesses of all samples are the same. In reality, the 9 samples have varying thicknesses ranging from 3.83 mm to 5.84 mm as determined by using a caliper to measure the sample heights. Similarly, the diameter of each sample was measured with a caliper so that the volume of each sample could be approximated as the volume of a cylinder whose height is equal to the thickness of the sample. Once the volume has been calculated, each sample can be weighed to determine its mass. Having each sample's mass and volume, the density can be found by dividing mass by volume.

The transmittance of each sample will be reported as the adjusted transmittance value at 550 nm. 550 nm was selected as the reporting wavelength because it falls approximately in the middle of the visible light spectrum, which spans 380-700 nm. Reporting the adjusted transmittance value at this wavelength gives the reader an idea of how much visible light is able to pass through each sample at a thickness of 2.2 mm.

The first sample, PT2_1_M, was not charged in a hydrothermal reactor, rather the vial alone was used as its polymerization vesicle. PT2_1_M was polymerized for 48 h at 120^{o}C and then for 3 more minutes at room temperature. The sample was then left to gel for 40 min at 80^{o}C,

and then was placed in the 100°C oven to age for 4 days. As determined by caliper measurements, the height and diameter of sample PT2_1_M were found to be 4.28 mm and 13.79 mm, respectively. The mass was found to be 0.3255 g; thus, the density was tabulated to be 0.509 g/cm^3. At 550 nm, the transmittance value adjusted to a thickness of 2.2 mm was found to be 78.89%.

Sample H1 9/25 was not charged in a hydrothermal reactor and polymerized in its vial for 47.5 h at 120°C. The sample was then gelled at 72°C for 1 h, then aged at 85°C for 4 days. The height and diameter of H1 9/25 were determined to be 4.27 mm and 14.07 mm by caliper measurements, and the sample was weighed to be 0.3463 g. Thus, the density was calculated to be 0.522 g/cm^3. When the transmittance spectrum was adjusted to reflect a sample thickness of 2.2 mm, the transmittance value at 550 nm was determined to be 77.90%.

Sample PT_1_HR_M was charged in a hydrothermal reactor and polymerized for 46 h at 120°, then further polymerized for 45 min at room temperature. The sample was allowed to gel for 1 h at 80°C, and then aged at 100°C for 4 days. Through caliper measurements, the sample's height and diameter were found to be 4.57 mm and 17.53 mm. When PT_1_HR_M was weighed, its mass was recorded as 0.5833 g. Therefore, its density was calculated to be 0.529 g/cm^3. At 550 nm, the transmittance value adjusted to a thickness of 2.2 mm was measured as 76.57%.

AH-44 was not charged in a hydrothermal reactor but polymerized in its vial for 48 h at 120°C. Following polymerization, the gelation and aging steps were combined into one step and were executed at 100°C for 4 days. The height and diameter of AH-44 were measured to be 5.36 mm and 14.46 mm using a caliper. The sample was weighed to be 0.4232 g, and its density was

calculated as 0.481 g/cm^3. At 550 nm, the transmittance value adjusted to a thickness of 2.2 mm was measured as 73.07%.

Sample PT_3_HR_M was charged in a hydrothermal reactor and polymerized for 48 h at 120^{o}C and then for 5 min at room temperature. The sample underwent gelation at 80^{o}C for 1 h, then aged at 100^{o}C for 4 days. As determined by caliper measurements, the height and diameter of PT_3_HR_M were determined to be 4.71 mm and 17.44 mm. When the sample was weighed, its mass was reported to be 0.5598 g. Therefore, the density of PT_3_HR_M was calculated to be 0.498 g/cm^3. At 550 nm, the transmittance value adjusted to a thickness of 2.2 mm was found to be 72.66%.

Sample AT_100_3_b was not charged in a hydrothermal reactor and was left to polymerize at 120^{o}C for 48 h. For this sample, the gelation and aging steps were combined into one step and this was executed at 95^{o}C for 4 days. AT_100_3_b had a reported adjusted transmittance value (to 2.2 mm) of 71.19% at 550 nm. The height and diameter of the sample were measured to be 4.13 mm and 13.53 mm by using a caliper. When weighed, AT_100_3_b was shown to have a mass of 0.3344 g, thus its density was calculated to be 0.563 g/cm^3.

Samples AH-43 and AH-47 were synthesized almost identically, as both were polymerized for 48.5 h at 120^{o}C without a hydrothermal reactor and then at room temperature for 7 min. Both were aged for 4 days at 100^{o}C but had different transmittance values at 550 nm when adjusted to having a thickness of 2.2 mm. AH-43 demonstrated an adjusted transmittance value of 68.60% at 550 nm, and the same adjusted value for AH-47 was found to be 62.42%.

It is important to note that the polymerization time and temperatures varied from sample to sample. The degree of polymerization was determined qualitatively by visual inspection for each sample. It is believed that the highest degree of polymerization could be obtained when the

sample was as viscous as possible without becoming solid. This is why each sample had varying polymerization times and temperatures. A high degree of polymerization is desired because it increases the number of hydrolysable sites [14]. Furthermore, Zu et al. found that a higher degree of polymerization was correlated with a higher degree of uniformity in the microstructure [14] which reduces the degree of light scattering and thus increases the light transmittance of the sample.

A summary of the synthesis techniques, transmittance adjusted to 2.2 mm at a wavelength of 550 nm, and density of each sample can be found in Table 1.

Table 1: Summary of PVPMS Aerogel Synthesis Results

Sample name	**Use of hydrothermal reactor**	**Polymerization time and temperature**	**Aging time and temperature**	**Density (g/cm^3)**	**Adjusted transmittance at 550 nm**
PT2_1_M	no	48 h at 120°C, 3 min ambient	40 min at 80°C, 4 d at 100°C	0.509	78.89%
H1 9/25	no	47.5 h at 120°C, 0 min ambient	1 h at 72°C, 4 d at 85°C	0.522	77.90%
PT_1_HR_M	yes	46 h at 120°C, 45 min ambient	1 h at 80°C, 4 d at 100°C	0.529	76.57%
AH-44	no	48 h at 120°C, 23 min ambient	4 d at 100°C	0.481	73.07%
PT_3_HR_M	yes	48 h at 120°C, 5 min ambient	1 h at 80°C, 4 d at 100°C	0.498	72.66%
AT_100_3_b	no	48 h at 120°C, 0 min ambient	4 d at 95°C	0.563	71.19%
AH-43	no	48.5 h at 120°C, 7 min ambient	4 d at 100°C	0.460	68.60%
AH-47	no	48.5 h at 120°C, 7 min ambient	4 d at 100°C	0.675	62.42%

Table *1* shows that the present study was able to reproduce the transmittance results of Zu et al. [14]. Figures 5 through 12 below show the transmittance spectra adjusted to reflect a

sample thickness of 2.2 mm for samples PT2_1_M, H1 9/25, PT_1_HR_M, AH-44, PT_3_HR_M, AT_100_3_b, AH-43, and AH-47, respectively. Note that in the following spectra, a black, dotted, vertical line represents the transmittance value at 550 nm.

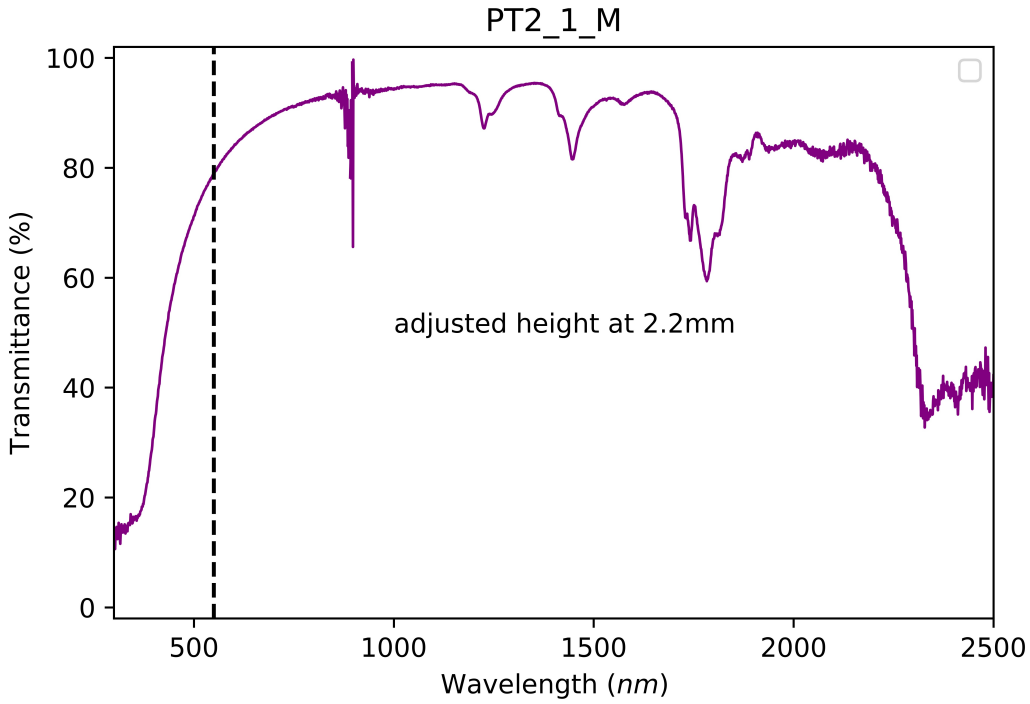

Figure 5: Adjusted transmittance spectrum for PT2_1_M

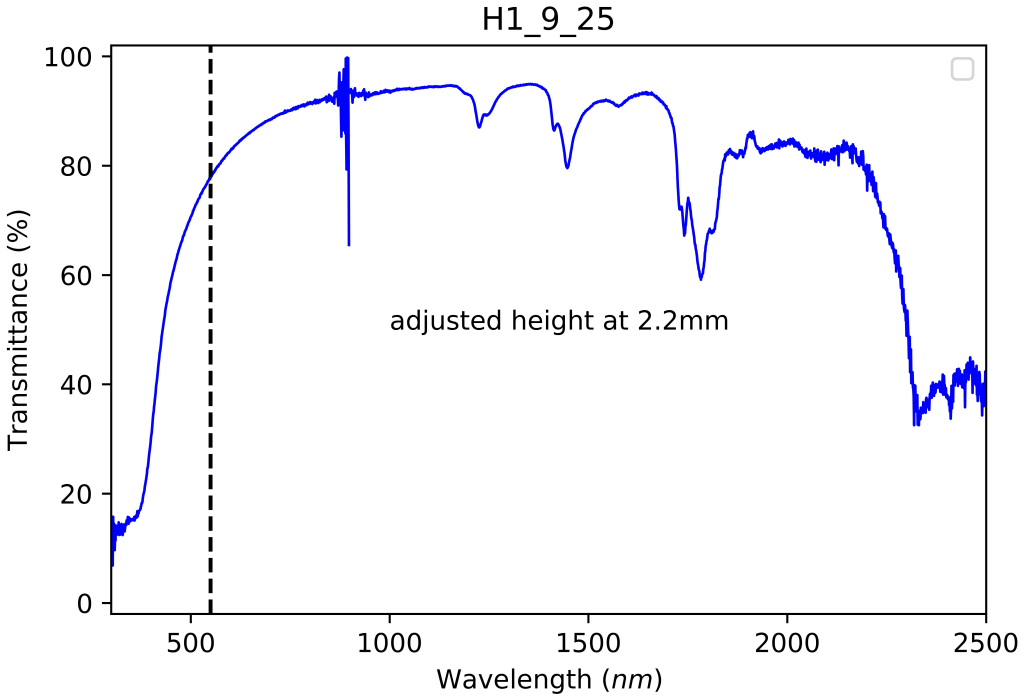

Figure 6: Adjusted transmittance spectrum for H1 9/25

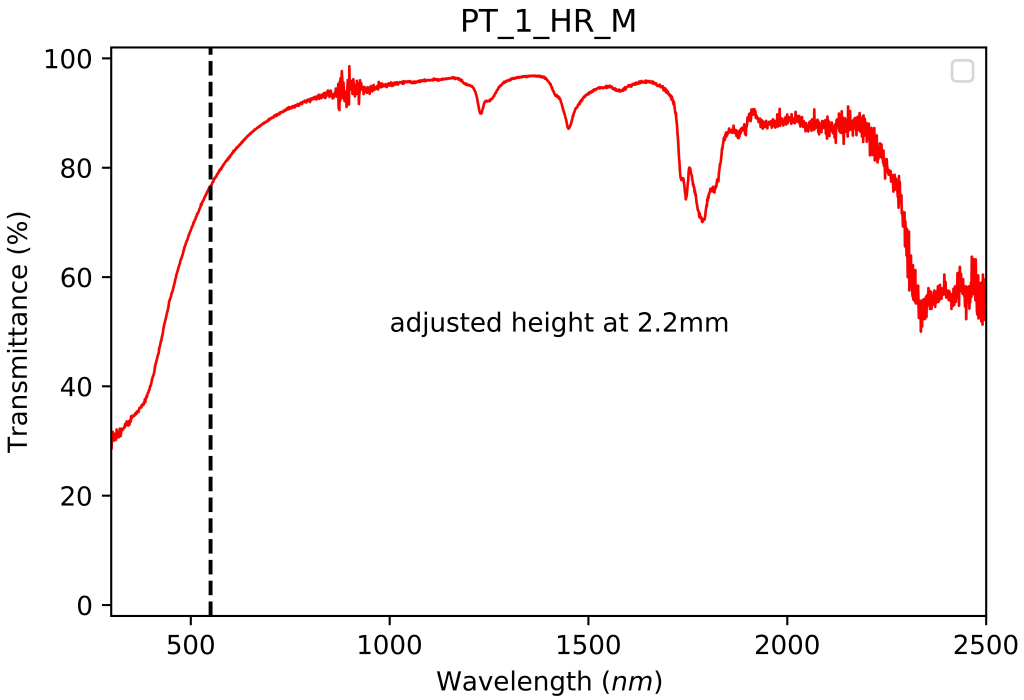

Figure 7: Adjusted transmittance spectrum for PT_1_HR_M

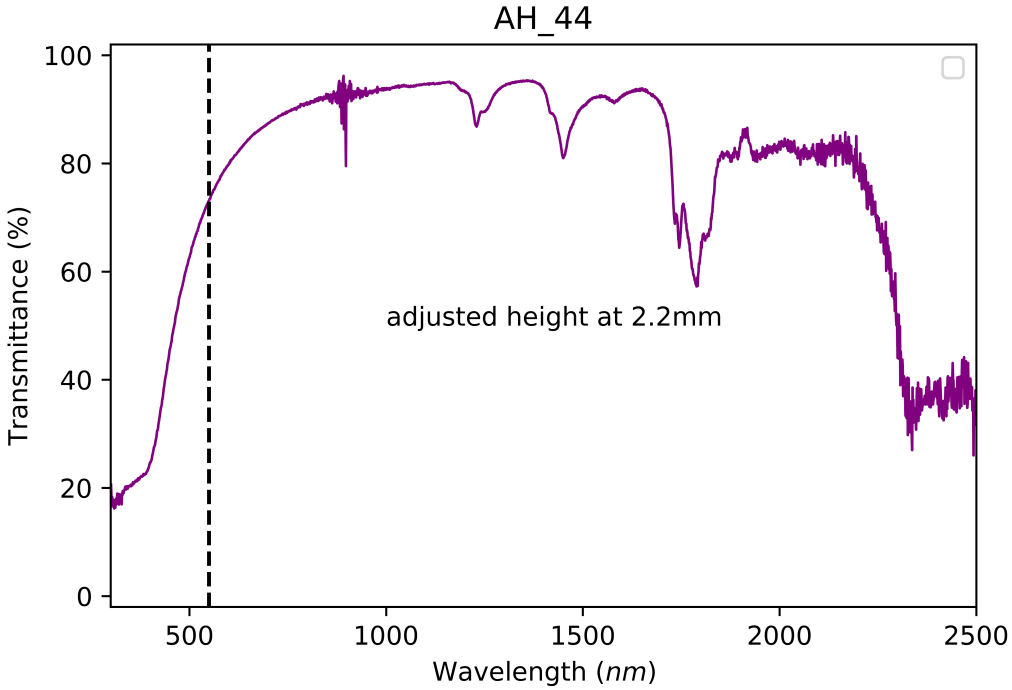

Figure 8: Adjusted transmittance spectrum for AH-44

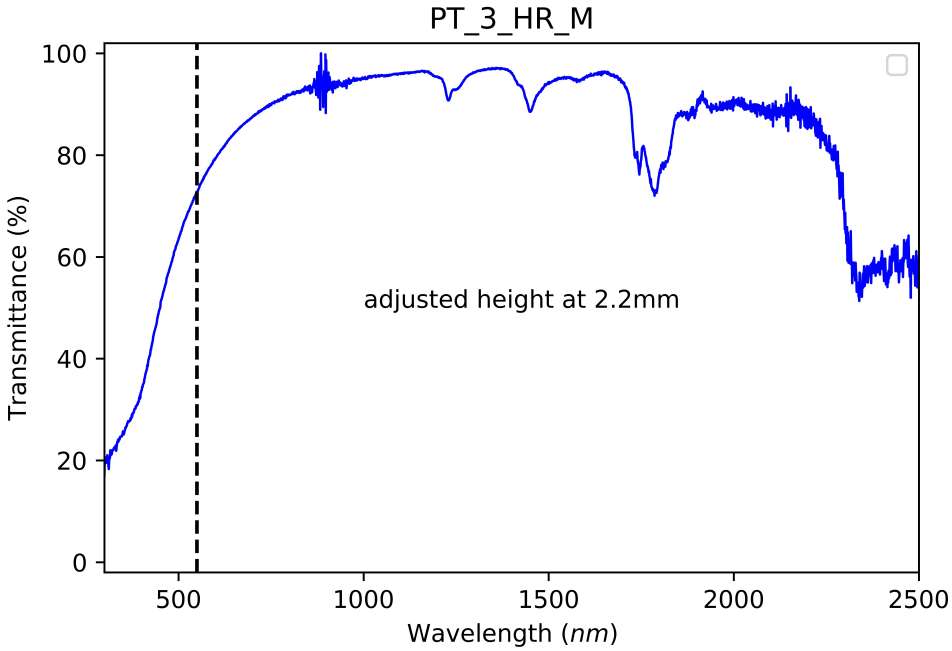

Figure 9: Adjusted transmittance spectrum for PT_3_HR_M

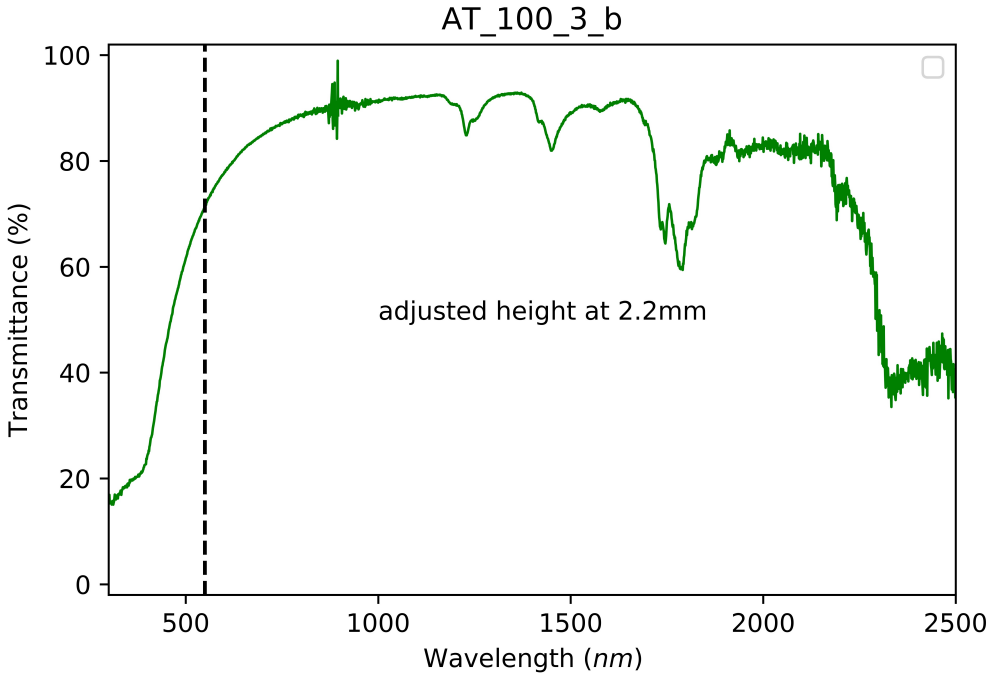

Figure 10: Adjusted transmittance spectrum for AT_100_3_b

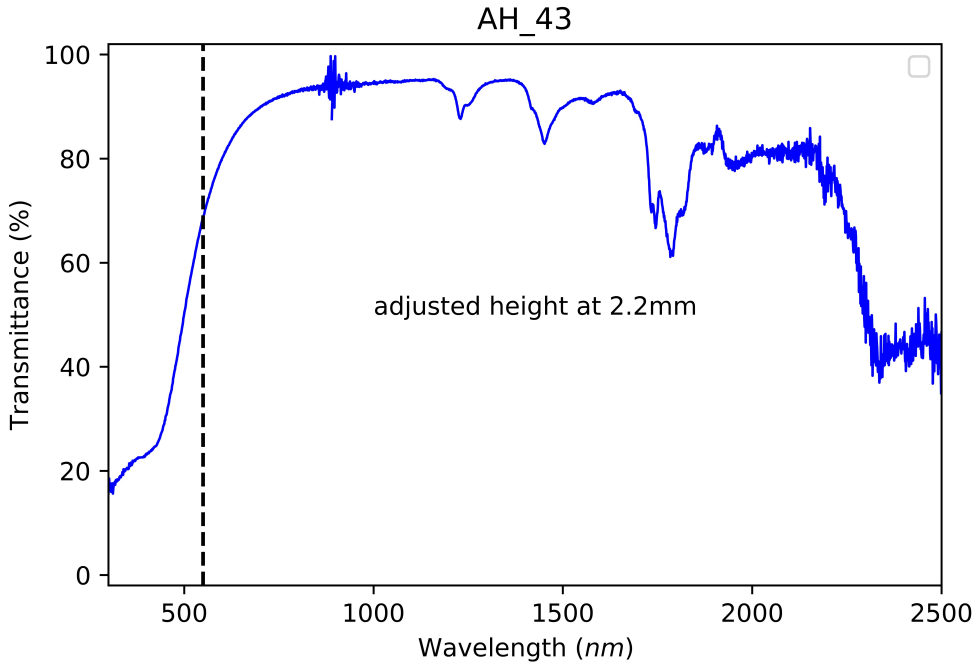

Figure 11: Adjusted transmittance spectrum for AH-43

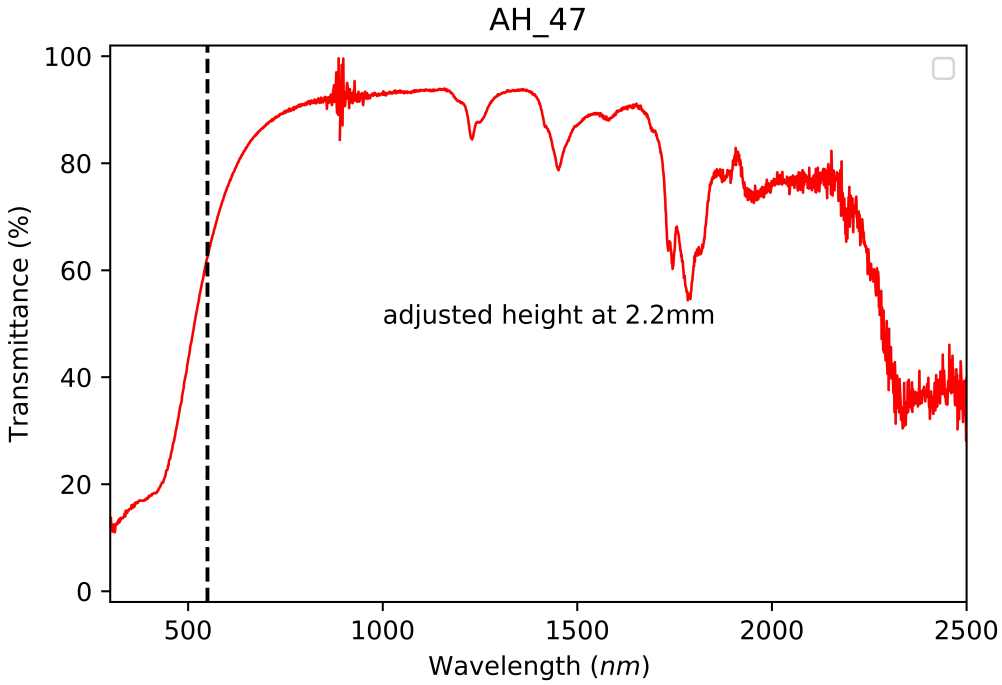

Figure 12: Adjusted transmittance spectrum for AH-47

RTE Forward Solution Results

Solving Equations 6-12 simultaneously using Python results in two contour plots. The first plot, shown in Figure 13, illustrates the trends in transmissivity (% transmittance divided by 100) as it changes with varying scattering albedo and optical thickness.

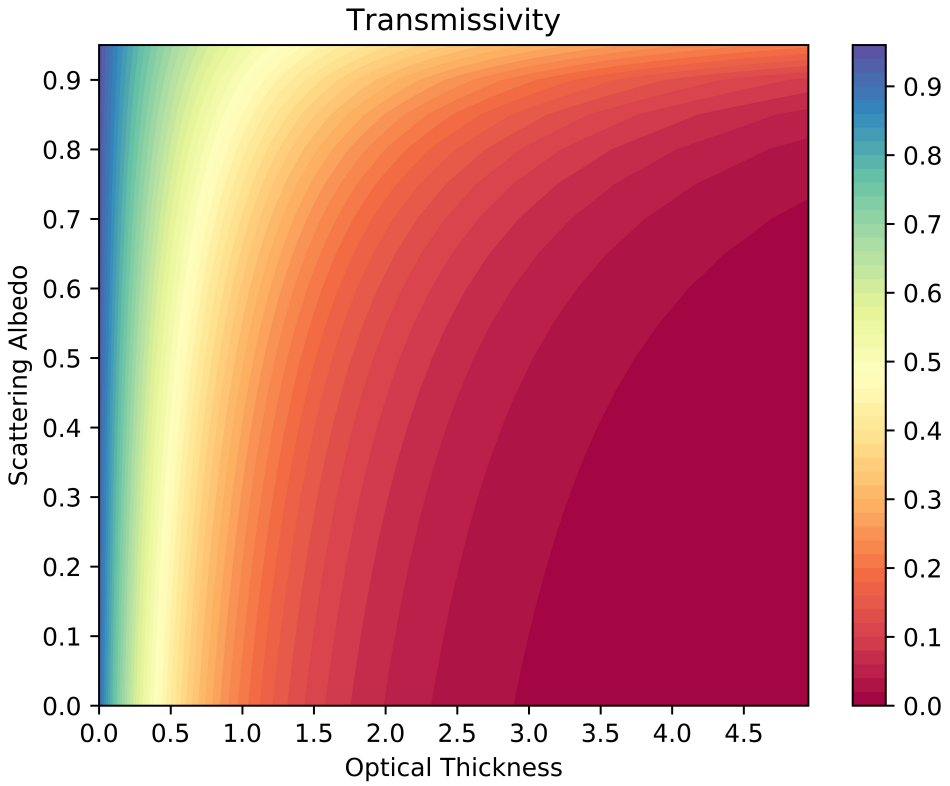

Figure 13: RTE forward solution: Transmissivity

As Figure 13 suggests, transmittance of light through a sample of aerogel increases slowly with scattering albedo when optical thickness is held constant. This result seems counterintuitive at first but can be explained using the definition of a Rayleigh scattering center. The pores and silica particles comprising the microstructure are both responsible for scattering incident light as it passes through a sample of aerogel. These pores and particles act as Rayleigh scattering centers, and as Figure 3 shows, Rayleigh scattering centers scatter incident light in all directions, including the forward direction, which contributes to transmittance. So, as the scattering albedo increases, the amount of light scattered in all directions also increases. Since transmittance is calculated as the sum of all exiting light, the amount of light scattered in the

forward direction contributes to this summation. Therefore, increased scattering albedo slightly increases the transmittance of light through a sample of aerogel.

Another observable trend from Figure 13 is the rapid reduction in transmittance with increasing optical thickness. Since optical thickness is directly correlated with the physical thickness of an aerogel sample, it follows that thicker samples will have lower transmittance values than thinner samples. Silica aerogel is a multiple scattering medium, so thicker samples will have a higher concentration of Rayleigh scattering centers (pores and particles). As the amount of Rayleigh scattering centers increases, the degree of scattered light will also increase, eventually reducing transmittance with thicker samples. At a critical thickness, there will be so many scattering points that no light will emerge from the medium at all. Therefore, increasing the sample thickness increases the optical thickness of the sample, which, in turn, will decrease the transmittance of the aerogel sample.

The second plot that can be generated from the forward solution to the RTE is shown in Figure 14. Figure 14 shows the variation in reflectivity (% reflectance divided by 100) with respect to both scattering albedo and optical thickness.

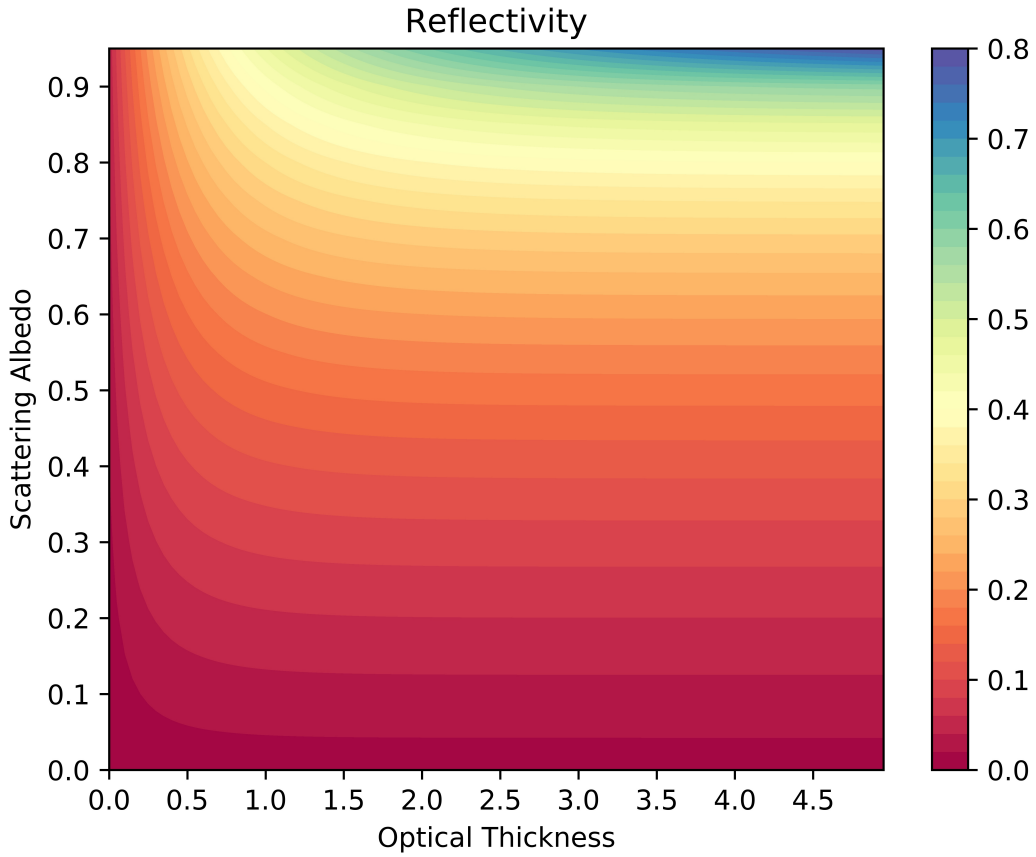

Figure 14: RTE forward solution: Reflectivity

Figure 14 shows that reflectivity rapidly increases as scattering albedo increases while holding optical thickness constant. As explained before, a higher scattering albedo indicates a higher degree of scattering of light by both pores and particles. Because the pores and particles responsible for scattering light act as Rayleigh scattering centers, they scatter light in all directions, as shown in Figure 3. Therefore, with a higher scattering albedo (and thus a higher degree of scattering), more light is scattered in both the forward direction (contributing to the transmittance of light) and the backward direction (contributing to the reflectance of light). Thus, as scattered albedo increases, so does both reflectance and transmittance, as shown by Figure 13 and Figure 14.

Figure 14 also shows that reflectance increases and then remains relatively constant as optical thickness increases for a certain scattering albedo. The region where reflectance increases with increasing optical thickness indicates that a thicker sample will reflect more light. This is because a thicker sample will have a larger number of scattering centers (both pores and particles, which comprise the aerogel microstructure). The large number of scattering centers present in a thicker sample will increase the amount of light scattered in the backward direction (as well as the forward direction) thus increasing the amount of reflected light.

Figure 15 below shows the calculated hemispherical transmittance (A) and hemispherical reflectance (B) as a function of optical thickness and scattering albedo done by Zhao et al. [15].

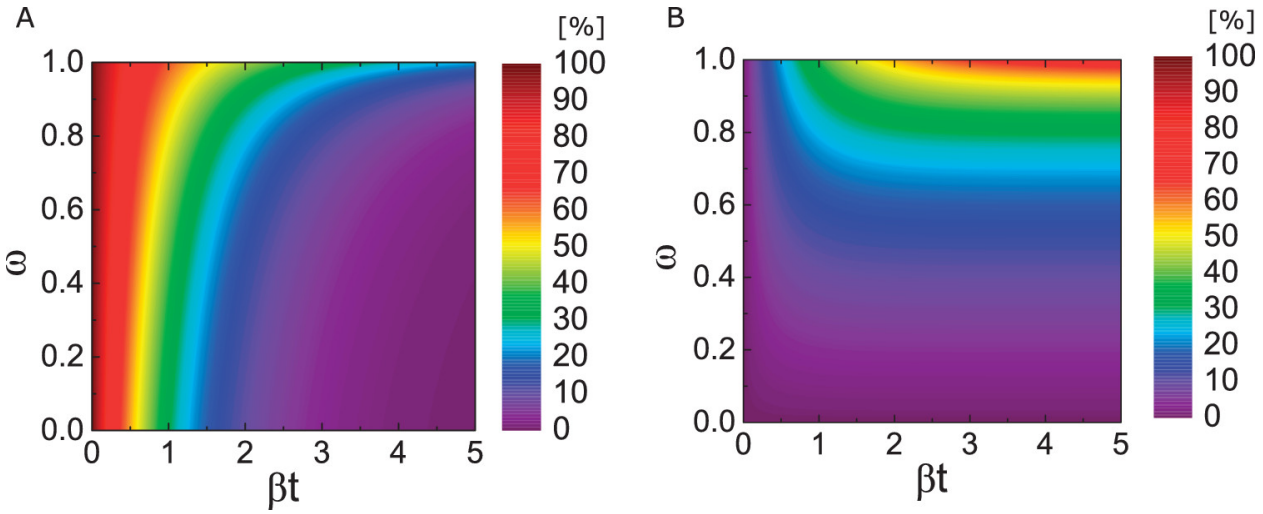

Figure 15: Zhao et al. calculated hemispherical transmittance (A) and hemispherical reflectance (B) as a function of optical thickness and scattering albedo *[15]*

By comparing the results presented in this work (shown in Figure 13 and Figure 14) and the results produced by Zhao et al., visual inspection reveals similarities in the two plots. Such similarities verify the accuracy of the hemispherical transmittance and reflectance calculated by the model of the present work.

Inherent Properties of TMOS Aerogel

Once experimental transmittance and reflectance data have been collected for TMOS aerogel, this data can be compared to the data maps produced by Figure 13 and Figure 14. Then, all points of intersection between the TMOS transmittance and reflectance data can be mapped and separated into x (scattering albedo, ω) and y (optical thickness, ξ) values. Dividing optical thickness by the physical thickness of the sample produces an extinction coefficient (β) data set. This particular TMOS aerogel sample was 7.3 mm thick. Therefore, the extinction coefficient can be plotted against the wavelengths measured, shown below in Figure 16.

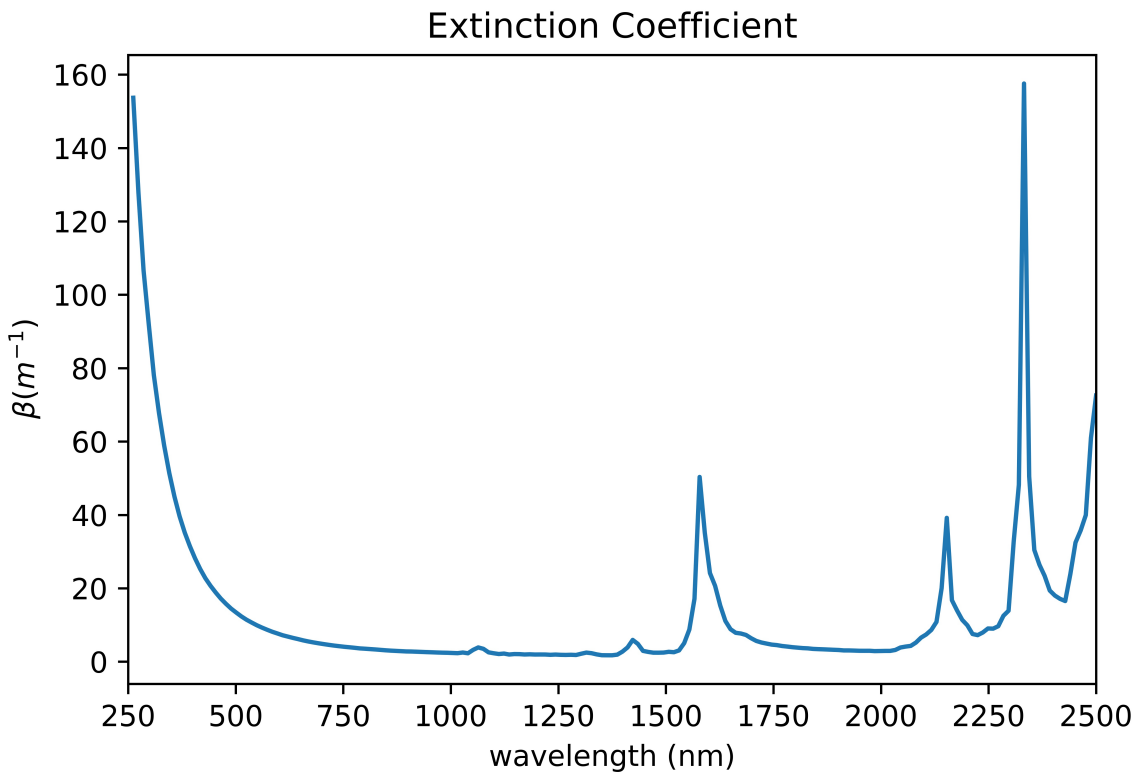

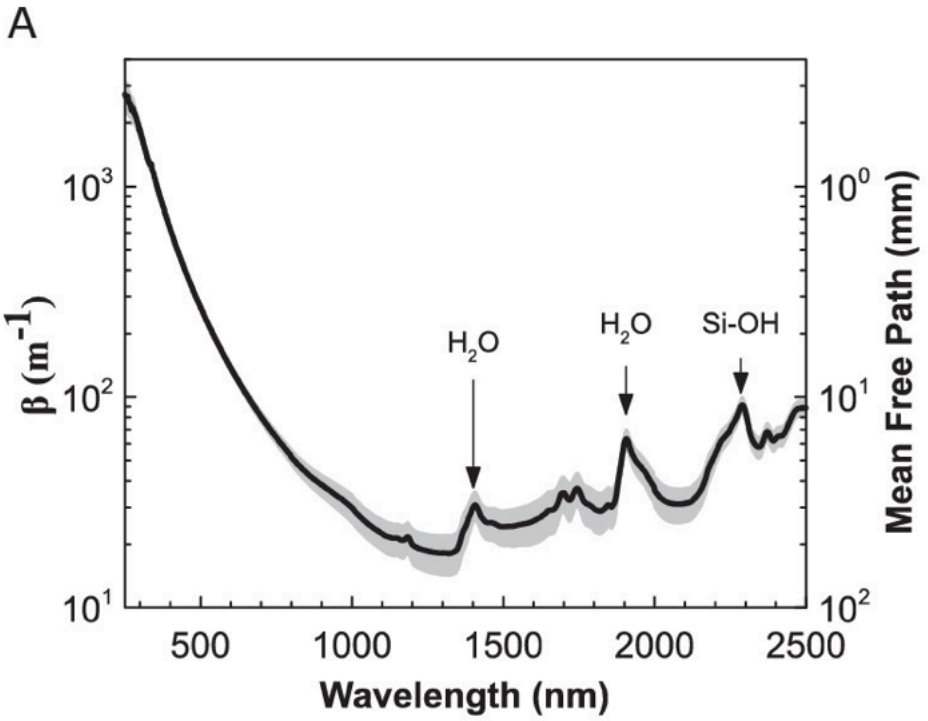

Figure 16: Extinction coefficient deduced by present work (top) and deduced by Zhao et al. *[15]* (bottom)

Figure 16 shows the extinction coefficient as a function of wavelength deduced by the present work (top) compared to that deduced by Zhao et al. [15] (bottom). The purpose of this comparison is to show that the extinction coefficient calculated in this work appears to behave similarly as a function of wavelength as compared to that calculated by Zhao et al. [15]. The similar behavior of the two plots shown in Figure 16 confirms that the model presented in this work is relatively accurate.

Figure 16 shows three distinct peaks around 1600 nm, 2100 nm, and 2300 nm. When measuring transmittance and reflectance data (from which, extinction coefficient is found), the aerogel sample is bombarded with radiation in the form of light. When the molecules of silica aerogel are subjected to a certain frequency of radiation that is equal to the frequency of vibration of one of its bonds, the molecule absorbs energy at that frequency [33]. Therefore, each

of the three peaks observed in Figure 16 correspond to the bending or stretching of certain bonds present in the aerogel. Studies have shown that the first two peaks around 1600 nm and 2100 nm show characteristics of the stretching and bending of water molecules [15] [34]. Finally, the peak around 2300 nm was determined in previous studies to represent the bending and stretching of silanol groups (Si-OH) [15] [34] indicating incomplete condensation of hydroxyl groups into siloxane bonds.

Similarly, the scattering albedo can be plotted against measured wavelength values as shown in Figure 17 below.

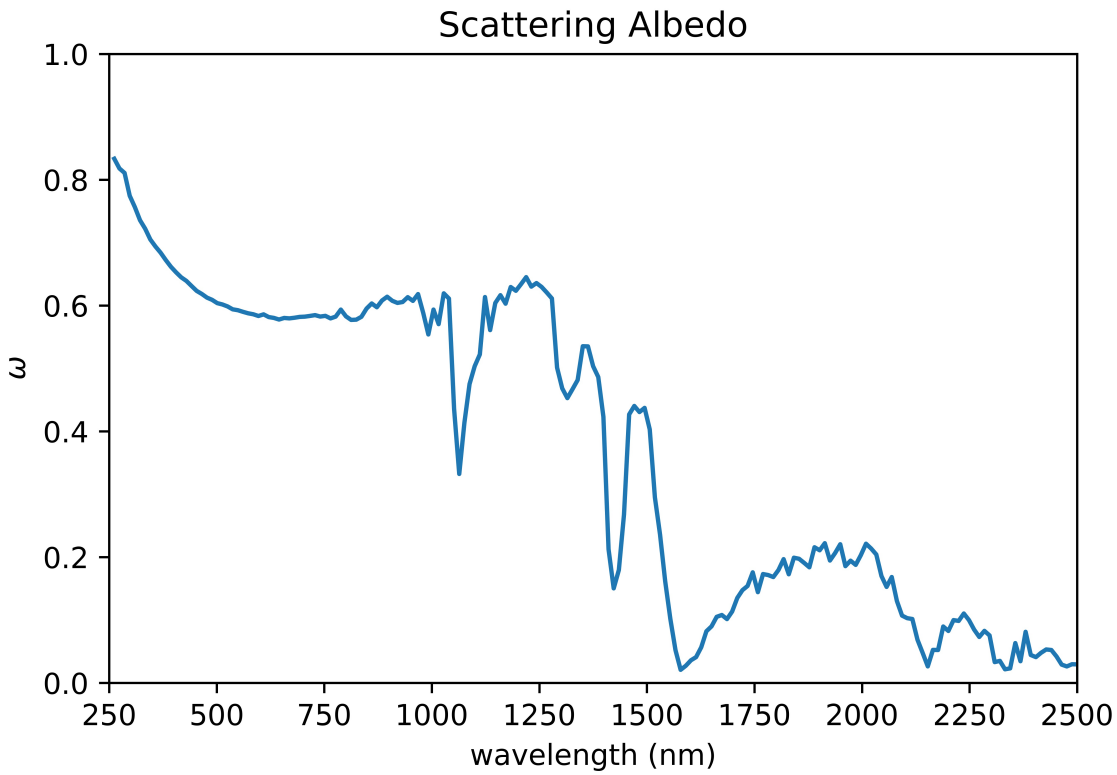

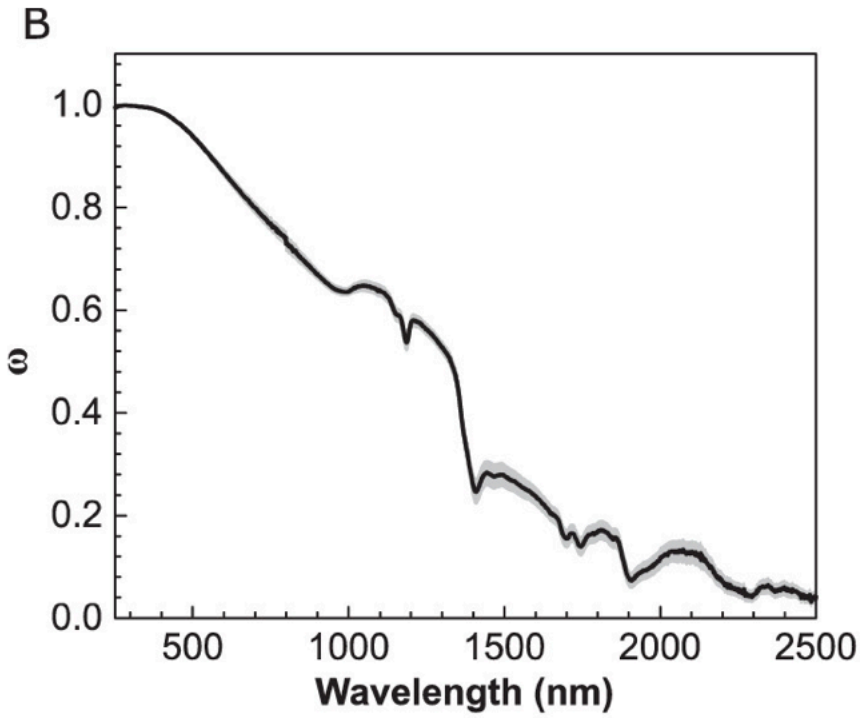

Figure 17: Scattering albedo deduced by present work (top) and by Zhao et al. (bottom) *[15]*

From the data mapped in Figure 16 and Figure 17, coefficients of scattering and absorption (σ_s and σ_a) can be calculated using Equations 9 and 10. Since both scattering albedo and optical thickness are wavelength-dependent quantities, the coefficients of scattering and absorption will be as well. To investigate the wavelength-dependence of extinction modes, the coefficients of scattering and absorption can be represented as a function of wavelength as shown in Figure 18.

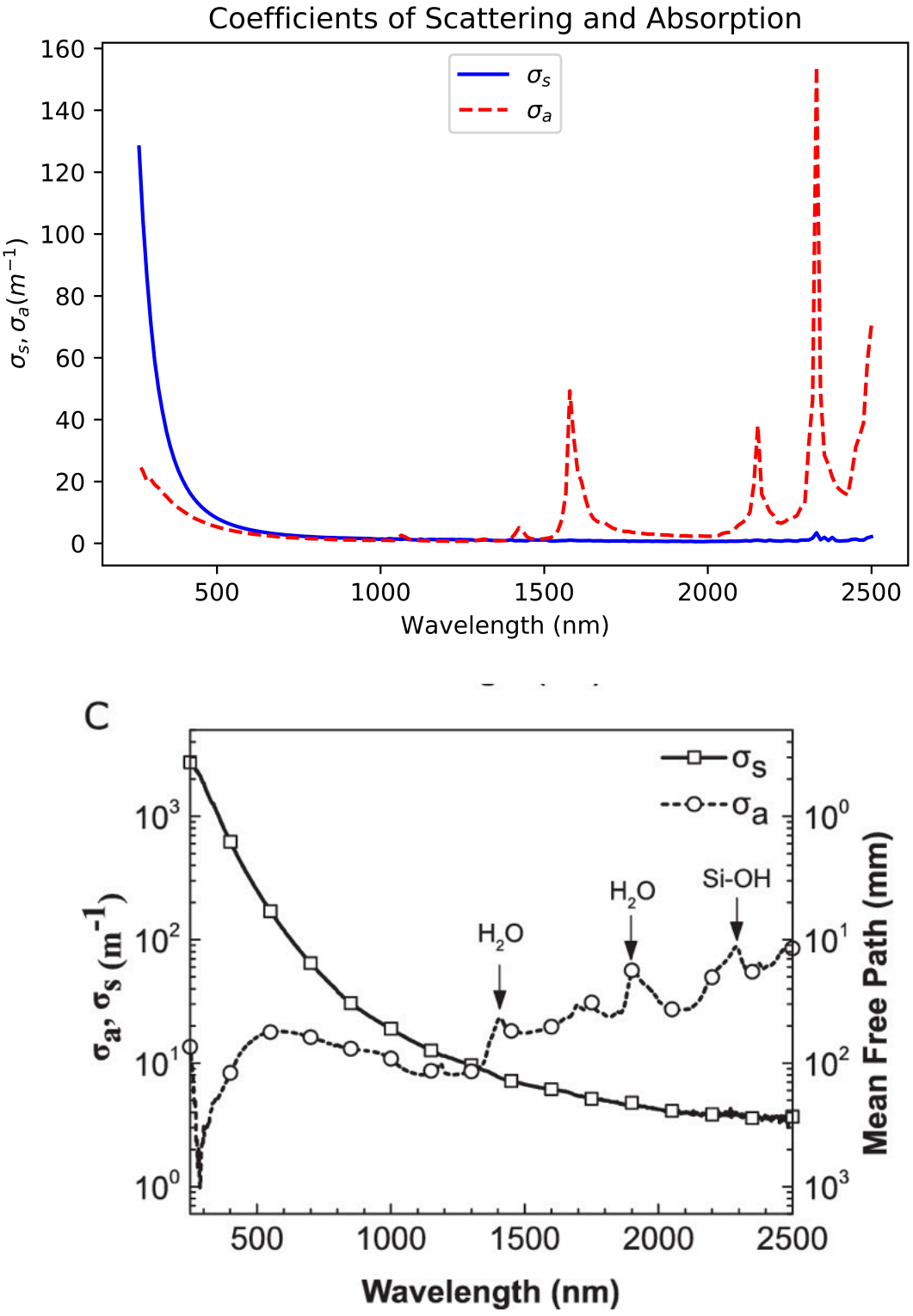

Figure 18: Coefficients of scattering and absorption deduced by present work (top) and by Zhao et al. (bottom) *[15]*

Figure 18 shows the coefficients of scattering and absorption deduced by the present work in the top figure and deduced by Zhao et al. in the bottom figure [15] as a function of wavelength. Comparing the results generated by the present work and by Zhao et al. reveals that the calculated coefficients of scattering and absorption behave similarly as a function of wavelength for both methods of deduction. Therefore, because of the similar behavior between the two plots, it can be concluded that the coefficients of scattering and absorption calculated by the present work are valid results to use for analysis.

In Figure 18, the scattering coefficient is shown to be rather large at shorter wavelengths, then, it rapidly decreases as the measured wavelength approaches 500 nm, and levels off to remain low for longer wavelengths. On the other hand, the absorption coefficient is particularly small at shorter wavelengths and decreases slightly between 250 and 500 nm. Then, the absorption coefficient peaks around 1600 nm, 2100 nm, and 2300 nm, reflecting the discrete vibration modes of water molecules and silanol groups [15] [34]. It is clear from Figure 18 that the scattering coefficient is significantly larger than the absorption coefficient at shorter wavelengths, and vice versa. Furthermore, the scattering albedo is higher in value between 250 and 750 nm, as depicted in Figure 17. These results imply that scattering is the dominant light extinction mode at shorter wavelengths (i.e., in the visible and UV band), and absorption is the dominant extinction mechanism at longer wavelengths.

Equation 24 is then used to calculate the scattering center diameter from the scattering coefficient data. For this sample of TMOS aerogel, the apparent density is 0.084 g/cm^3, the density of SiO_2 is 2.2 g/cm^3, and the relative refractive index of silica to air is 1.46. The scattering center diameter can be graphed as a function of wavelength, as shown in Figure 19.

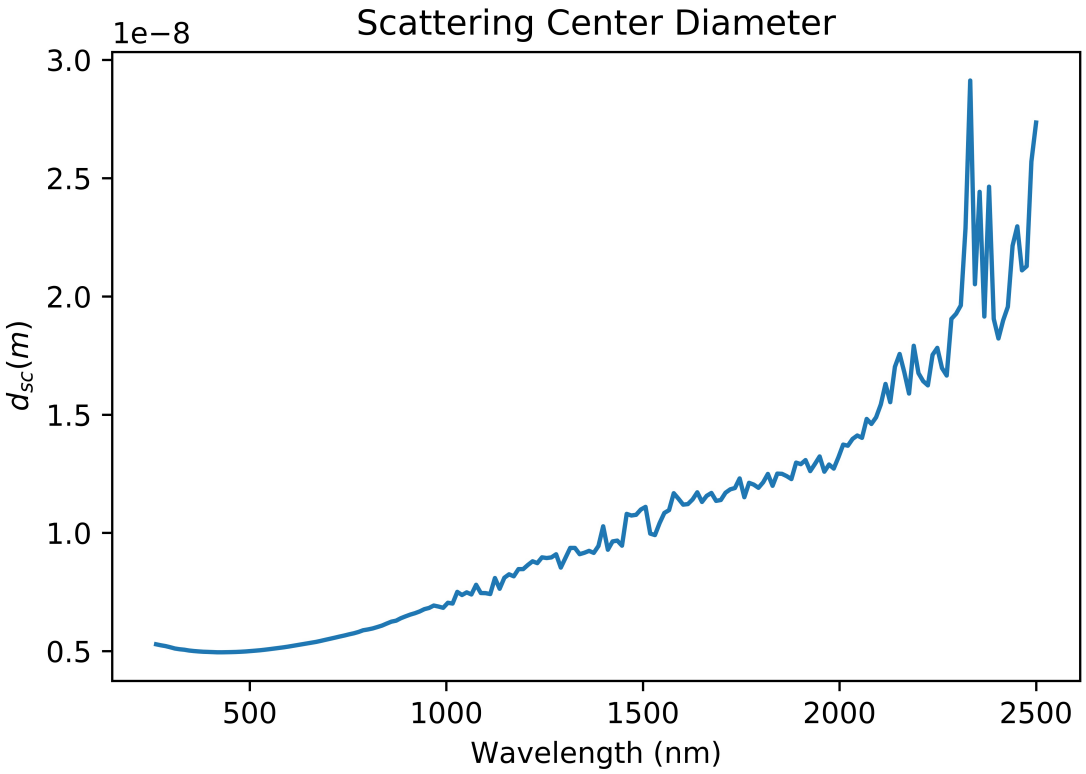

Figure 19: Scattering center diameter plot

Figure 19 shows that the effective scattering center diameter is a smooth function of wavelength from 250 nm to about 1000 nm. Beyond this range, the function of scattering center diameter with respect to wavelength becomes increasingly noisy. This observation is explained by the fact that light extinction is scattering-dominant at smaller wavelengths, where the function is observed to be smooth. The dominant light extinction mechanism at longer wavelengths is absorption, not scattering, where the function is observed to be noisy. Thus, at longer wavelengths, where the attenuation of light is mainly due to absorption, calculating the effective scattering center diameter may not be applicable.

Future work on this project includes applications of the methods used to produce Figure 19. First, the scattering center diameter data plotted in Figure 19 should be verified using small-angle X-ray scattering (SAXS). Once this has been done, regression analysis can be performed on the scattering center data set to deduce a simpler trend of d_{sc} as a function of wavelength. Furthermore, the scattering diameter sizes can be compared to the transmittance of a sample at a single wavelength or over a certain range of wavelengths. Then, it will be possible to identify how different scattering center sizes change the transmittance of a particular sample, and vice versa. If it is known how transmittance is related to scattering center diameter, it will then be possible to predict d_{sc} of a sample simply from its experimentally measured transmittance spectra. This type of model will eliminate the need for the SAXS method of determining scattering center diameter. The ability to determine the scattering center diameter from experimentally measured transmittance data allows one to gain deeper insight into the microstructure of samples prepared using different synthesis techniques. In theory, some synthesis technique could be implemented to produce a sample of certain transmittance and with a certain scattering center diameter. Having this information will allow for the optimization of the transmittance of a particular type of aerogel.

Conclusion

This study was successful in synthesizing ambiently dried polyvinylpolymethyl siloxane aerogel using the one-step, base-catalyzed hydrolysis and condensation method described by Zu et al. [14]. The method of synthesis detailed in this report was successful in producing monolithic PVPMS aerogel samples with adjusted transmittance values (at 550 nm, to reflect a

sample thickness of 2.2 mm) ranging 62.42-78.89%. Furthermore, the samples produced via this method were found to have densities from 0.460 g/cm^3 to 0.675 g/cm^3.

This study was also successfully able to solve the 1-D radiative transfer equation for the intensity field of light scattered by a porous medium and subsequently calculate the hemispherical transmittance and reflectance as functions of scattering albedo and optical thickness. The contour plots representing these functions were found to agree with results found by Zhao et al. Comparing these data maps to the experimentally measured transmittance and reflectance data of TMOS aerogel samples allows for the deduction of the inherent properties of scattering albedo and extinction coefficient. The deduced scattering albedo and extinction coefficient were plotted against wavelength and compared to the results of Zhao et al. The comparison revealed that the scattering albedo and extinction coefficient deduced by the present work and by Zhao et al. behaved similarly as functions of wavelength.

Equations 9 and 10 were then used to calculate the coefficients of scattering and absorption from the deduced scattering albedo and extinction coefficient. These coefficients were plotted against wavelength, compared to the results of Zhao et al., and were found to agree in behavior. It was also found that the scattering coefficient was both a smooth function of wavelength and significantly larger than the absorption coefficient at smaller wavelengths. The absorption coefficient was found to be quite low at smaller wavelengths with high distinct peaks at longer wavelengths. This means that scattering is the dominant light extinction mechanism at smaller wavelengths, namely, in the UV-visible band. Similarly, absorption is the dominant mode of extinction at higher wavelengths due to the absorption of energy by water and silanol groups, which are responsible for producing the distinct peaks in the plot.

Finally, Equation 24 was used along with the deduced scattering coefficient to calculate the effective scattering center diameter as a function of wavelength. It was found that the scattering center diameter is a smooth function of wavelength from 250-1000 nm. This is due to the fact that scattering is the dominant extinction mechanism for small wavelengths. Future work includes applying this method of deducing the scattering center diameter to PVPMS aerogel samples to replace finding the scattering size via SAXS analysis. Moreover, the model will also be used to determine trends between scattering center diameter and transmittance. From there, it will be possible to understand how various synthesis techniques affect the microstructure of the final product from its experimentally measured transmittance and reflectance data, making it possible to optimize the transmittance of PVPMS aerogel samples.

References

[1] S. S. Kistler, "Coherent Expanded Aerogels," *The Journal of Physical Chemistry,* 1932.

[2] A. Soleimani et al., "Silica aerogel; synthesis, properties, and characterization," *Journal of Materials Processing Technology,* vol. 199, 2007.

[3] Guoyou Wu et al., "Preparation and surface modification mechanism of silica aerogels via ambient pressure drying," *Materials Chemistry and Physics,* vol. 129, no. 1-2, pp. 308-314, 2011.

[4] Lee A. Weinstein et al., "A Hybrid Electric and Thermal Solar Receiver," *Joule,* vol. 2, pp. 962-975, 2018.

[5] Elise Strobach et al., "High temperature stability of transparent silica aerogels for solar thermal applications," *APL Materials,* vol. 7, 2019.

[6] Lee A. Weinstein et al., "Concentrating Solar Power," *Chemical Reviews,* 2015.

[7] Michael Rubin et al., "Transparent silica aerogels for window insulation," *Solar Energy Materials,* vol. 7, no. 4, pp. 393-400, 1983.

[8] C. Buratti, E. Moretti, "Glazing systems with silica aerogel for energy savings in buildings," *Applied Energy,* vol. 98, pp. 396-403, 2012.

[9] AbuBakr Bahaj et al., "Potential of emerging glazing technologies for highly glazed buildings in hot arid climates," *Building Energy,* 2008.

[10] Kaushika ND et al., "Solar transparent insulation materials: a review," *Renewable Sustainable Energy Reviews,* vol. 7, pp. 317-351, 2003.

[11] Jyoti L. Gurav et al., "Silica Aerogel: Synthesis and Applications," *Journal of Nanomaterials,* 2010.

[12] J. C. Brinker, Sol-Gel Science: The Physics and Chemistry of Sol-Gel Processing, San Diego, CA: Academic Press, 1990.

[13] Taiyo Shimizu et al., "Transparent Ethylene-Bridged Polymethylsiloxane Aerogels and Xerogels with Improved Bending Flexibility," *Langmuir,* no. 32, pp. 13427-13434, 2016.

[14] Guoqing Zu et al., "Transparent, Superflexible Doubly Cross-Linked Polyvinylpolymethylsiloxane Aerogel Superinsulators via Ambient Pressure Drying," *ACS Nano,* no. 12, pp. 521-532, 2018.

[15] Lin Zhao, Sungwoo Yang et al., "Modeling silica aerogel optical performance by determining its radiative properties," *AIP Advances,* no. 6, 2016.

[16] Subramaniam Iswar et al., "Effect of aging on silica aerogel properties," *Microporous and Mesoporous Materials,* pp. 293-302, 2017.

[17] Pradip B. Sarawade et al., "Influence of Solvent Exchange on the Physical Properties of Sodium Silicate Based Aerogel Prepared at Ambient Pressure," *Aerosol and Air Quality Research,* vol. 6, no. 1, pp. 93-105, 2006.

[18] George W. Sherer, "Theory of Drying," *Jornal of the American Ceramic Society,* vol. 73, no. 1, pp. 3-14, 1990.

[19] Tomasz Blaszczyński et al., "Synthesis of Silica Aerogel by Supercritical Drying Method," *Procedia Engineering,* vol. 57, pp. 200-206, 2013.

[20] Qifeng Chen et al., "Preparation and Characterization of Silica Aerogel Microspheres," *Materials,* vol. 10, 2017.

[21] A. Emmerling et al., "Relationship between optical transparency and nanostructural features of silica aerogels," *Jounral of Non-Crystalline Solid,* vol. 185, no. 3, pp. 240-248, 1995.

[22] P. Wang et al., "Optical investigations of silica aerogels," *Journal of Non-Crystalline Solids,* vol. 145, pp. 141-145, 1992.

[23] K. S. N.D. Kaushika, "Solar transparent insulation materials: a review," *Renewable and Sustainable Energy Reviews,* vol. 7, no. 4, pp. 317-351, 2003.

[24] C.F. Boren, D.R. Huffman, Absorption and Scattering of Light by Small Particles, Wiley, 1983.

[25] M. Modest, Radiative Heat Transfer, Oxford: Academic Press, 2013.

[26] David L. Andrews, "Rayleigh Scattering and Raman Spectroscopy," in *Encylopedia of Spectroscopy and Spectrometry*, 1999.

[27] A. J. Hunt, "Light scattering for aerogel characterization," *Journal of Non-Crystalline Solids,* vol. 225, pp. 303-306, 1998.

[28] Haitong Yu et al., "Calculation and experimental validation of spectral properties of microsize grains surrounded by nanoparticles," *Optics Express,* vol. 22, no. 7, pp. 7925-7930, 2014.

[29] G.R. Cunnington, S.C. Lee, "Radiative Properties of Fiber-Reinforced Aerogel: Theory Versus Experiment," *Journal of Thermophysics and Heat Transfer,* vol. 12, no. 1, 1998.

[30] Lin Zhao et al., "Harnessing Heat Beyond 200 C from Unconcentrated Sunlight with Nonevacuated Transparent Aerogels," *ACS Nano,* vol. 13, no. 7, 2019.

[31] V.A. Bhanu, K. Kishore, "Role of oxygen in polymerization reactions," *Chemical Reviews,* vol. 91, no. 2, pp. 99-117, 1991.

[32] Sukbinder Singh, "Sukhbinder Intersection," GitHub, 10 April 2017. [Online]. Available: github.com/sukhbinder/intersection. [Accessed January 2020].

[33] P. Y. Bruice, "Infrared Spectroscopy," in *Organic Chemistry*, Pearson Educations, 2017.

[34] E. Stolper, "Water in silicate glasses: An infrared spectroscopic study," *Contributions to Mineralogy and Petrology,* vol. 81, pp. 1-17, 1982.